Atmospheric
Chemistry
and Physics
Discussions

Open Access

Forecasting global atmospheric CO_2

A. Agustí-Panareda[1], S. Massart[1], F. Chevallier[2], S. Boussetta[1], G. Balsamo[1], A. Beljaars[1], P. Ciais[2], N. M. Deutscher[3], R. Engelen[1], L. Jones[1], R. Kivi[4], J.-D. Paris[2], V.-H. Peuch[1], V. Sherlock[2], A. T. Vermeulen[5], P. O. Wennberg[6], and D. Wunch[6]

[1]European Centre for Medium-Range Weather Forecasts, Reading, UK
[2]Laboratoire des Sciences du Climat et l'Environnement, CEA-CNRS-UVSQ, IPSL, Gif sur Yvette, France
[3]Institute of Environmental Physics, Bremen, Germany
[4]Finnish Meteorological Institute, Sodankylä, Finland
[5]Energy research Center of the Netherlands, Petten, the Netherlands
[6]California Institute of Technology, Pasadena, CA, USA

Correspondence to: A. Agustí-Panareda (anna.agusti-panareda@ecmwf.int)

ACPD

14, 13909–13962, 2014

Global CO_2 forecast

A. Agustí-Panareda et al.

Title Page

Abstract	Introduction
Conclusions	References
Tables	Figures

◄◄   ►►

◄   ►

Back   Close

Full Screen / Esc

Printer-friendly Version

Interactive Discussion

Abstract

A new global atmospheric carbon dioxide (CO_2) real-time forecast is now available as part of the pre-operational Monitoring of Atmospheric Composition and Climate – Interim Implementation (MACC-II) service using the infrastructure of the European Centre for Medium-Range Weather Forecasts (ECMWF) Integrated Forecasting System (IFS). One of the strengths of the CO_2 forecasting system is that the land surface, including vegetation CO_2 fluxes, is modelled online within the IFS. Other CO_2 fluxes are prescribed from inventories and from off-line statistical and physical models. The CO_2 forecast also benefits from the transport modelling from a state-of-the-art numerical weather prediction (NWP) system initialized daily with a wealth of meteorological observations. This paper describes the capability of the forecast in modelling the variability of CO_2 on different temporal and spatial scales compared to observations. The modulation of the amplitude of the CO_2 diurnal cycle by near-surface winds and boundary layer height is generally well represented in the forecast. The CO_2 forecast also has high skill in simulating day-to-day synoptic variability. In the atmospheric boundary layer, this skill is significantly enhanced by modelling the day-to-day variability of the CO_2 fluxes from vegetation compared to using equivalent monthly mean fluxes with a diurnal cycle. However, biases in the modelled CO_2 fluxes also lead to accumulating errors in the CO_2 forecast. These biases vary with season with an underestimation of the amplitude of the seasonal cycle both for the CO_2 fluxes compared to total optimized fluxes and the atmospheric CO_2 compared to observations. The largest biases in the atmospheric CO_2 forecast are found in spring, corresponding to the onset of the growing season in the Northern Hemisphere. In the future, the forecast will be re-initialized regularly with atmospheric CO_2 analyses based on the assimilation of CO_2 satellite retrievals, as they become available in near-real time. In this way, the accumulation of errors in the atmospheric CO_2 forecast will be reduced. Improvements in the CO_2 forecast are also expected with the continuous developments in the operational IFS.

1   Introduction

Atmospheric composition monitoring was integrated in the Numerical Weather Prediction framework (NWP) at the European Centre for Medium-Range Weather Forecasts (ECMWF) as part of the Global and regional Earth-System Monitoring using Satellite and in situ data (GEMS) and the Monitoring of Atmospheric Composition and Climate (MACC) projects (Hollingsworth et al., 2008). The resulting global forecasting system of atmospheric composition benefits from the existing operational infra-structure for weather forecasting, satellite data assimilation and high performance computing at ECMWF. Until recently, only forecasts of reactive gases and aerosols were provided in near-real time on a routine basis (Flemming et al., 2009; Morcrette et al., 2009) as part of the Copernicus European programme, formerly called GMES (Global Monitoring for Environment and Security). The reasons for not having carbon dioxide (CO$_2$) stemmed from the challenges associated with modelling the CO$_2$ fluxes and the relatively small signals characterizing CO$_2$ variability making the accuracy requirements for the model simulations more stringent than for other trace gases. The recent addition of the CTESSEL Carbon module in the operational Integrated Forecasting System (IFS) at ECMWF (Boussetta et al., 2013a) has now also made feasible the delivery of atmospheric CO$_2$ forecasts in real time. Although the forecast is currently not initialized with a CO$_2$ analysis because of the lack of CO$_2$ observations with global coverage in near-real time, it relies heavily on a wealth of meteorological observations for initializing the meteorology and transport. Moreover, we expect that in the near future there will be satellite retrievals of CO$_2$ from GOSAT and OCO-2 available a few days behind real time. These retrievals will be assimilated to produce CO$_2$ analyses also in near-real time. It is worth noting that the CO$_2$ retrievals provide averaged column information of CO$_2$ and only for clear-sky conditions. Therefore, they cannot provide information on the CO$_2$ vertical distribution nor the CO$_2$ anomalies associated with cloudy regions within convective and synoptic weather systems. Thus, the CO$_2$ forecast model will be crucial in filling this information gap during the data assimilation process.

The atmospheric CO_2 variability results mainly from a strong synergy between surface fluxes and atmospheric transport. The advection of CO_2 across meridional gradients associated with large-scale flux patterns dominates the variability in the free troposphere, whereas local fluxes also play a role in the variability of atmospheric CO_2 close to the surface, i.e. within the atmospheric boundary layer (Keppel-Aleks et al., 2011, 2012). Modelling the spatial and temporal CO_2 variability is a challenging task. The difficulties arise from uncertainties in the modelling of both the sources/sinks (le Quéré et al., 2009) and transport (Law et al., 2008a, b).

Globally, the CO_2 variability on time scales ranging from diurnal, seasonal, to interannual is dominated by the terrestial biogenic fluxes (Geels et al., 2004). The challenge of modelling the terrestrial biogenic fluxes comes from high spatial heterogeneity of the land surface and complex processes with large uncertainties. Some of these uncertainties stem from a lack of observational data with sufficient global coverage to characterize all the variability in space and time associated with vegetation and carbon pools. At the same time, the biospheric fluxes are strongly influenced by climate variability (Keeling et al., 1995). Therefore, the timely availability of accurate meteorological datasets is also crucial. The recent development of the CTESSEL Carbon module within the IFS takes advantage of accurate real-time climate forcing in order to provide online terrestrial biogenic fluxes also in real time.

The online computation of terrestrial biogenic fluxes and transport – both forced and initialized by NWP analyses – is key to ensure consistency in the coupling between fluxes and transport. An example of the importance of this consistency is the passage of mid-latitude frontal cyclones. The change in radiation associated with the frontal cloud reduces the photosynthetic CO_2 uptake which results in a substantial increase in atmospheric CO_2 (~ 10 ppm) near the surface, as respiration continues to emit CO_2 (Chan et al., 2004). This high-CO_2 anomaly can then be transported by frontal ascent to the mid and upper troposphere. This coupling between fluxes and transport also works on a seasonal scale. Meridional transport by mid-latitude frontal cyclones reduces/amplifies the seasonal cycle at mid/high latitudes (Parazoo et al., 2011). On

diurnal scales and seasonal time scales, there is a covariance between turbulent mixing in the planetary boundary layer and terrestrial biogenic fluxes known as the rectifier effect (Denning et al., 1999).

In addition to the modelling challenges, the availability of CO_2 observations is central to be able to provide optimal estimates of CO_2 concentrations and fluxes, as well as error estimates of the CO_2 model forecasts. So far, the most accurate CO_2 observations are from in situ measurements close to the surface. In the past, these have been available with a delay of 1 to 2 years. This long delay in the availability of observations – combined with the large uncertainties in modelling of fluxes, their forcings, and the transport model – has hindered the task of providing CO_2 information in a timely manner. However, recently, the Integrated Carbon Observation System (ICOS) observing network started to provide continuous in situ CO_2 observations with a 1 day lag as part of their pre-operational phase. Currently, there are 7 stations in the pre-operational network. Some of these stations are sampling baseline air, and therefore allow a continuous monitoring of the background bias in the CO_2 forecast.

The aim of this paper is to document the capabilities and limitations of this real time CO_2 forecast, currently available with a 5 day lead time. This is done by comparing CO_2 hindcasts – i.e model simulations for the past 10 years using the same configuration as the real-time CO_2 forecast – with a wide range of independent observations, thus, giving an assessment of the representation of the CO_2 spatial and temporal variability at different scales. Furthermore, the continuous automated monitoring of the atmospheric CO_2 forecast with ICOS observations is also shown. This evaluation supports the ongoing monitoring of the model errors. It is also the first step towards being able to assimilate CO_2 observations in near-real time.

The paper is structured as follows. The description of the model CO_2 fluxes and transport is presented in Sect. 2. The evaluation of the CO_2 hindcasts is done in Sect. 3 by using observations from the Integrated Carbon Observation System (ICOS), the Total Carbon Column Observing Network (TCCON), the National Oceanic and Atmospheric Administration (NOAA) networks and the HIAPER Pole to Pole Observations

(HIPPO) field experiment. The CO_2 hindcast performance is dicussed in Sect. 4, high-lighting future work to reduce the errors as part the operational upgrades of the system. Finally, Sect. 5 recaps on the CO_2 forecast capabilities and possible applications.

2 Forecast configuration and model description

5   This section presents the CO_2 forecast set-up, including a description of the transport and flux components in the model. The CO_2 modelling is done within the NWP framework, using the IFS model from ECMWF. Both transport and terrestrial biogenic carbon fluxes are computed online and other prescribed fluxes are read from inventories. This ensures a consistency between flux resolution and transport resolution and it
10   also allows a full coupling between meteorological forcing of biogenic fluxes and transport. A description of the main features of the IFS transport are provided in Sect. 2.1. Section 2.2 describes the different fluxes included in the model in more detail.

  In order to be able to evaluate the CO_2 forecast over different time scales, yearly CO_2 hindcasts were performed from 2003 to 2012. The hindcasts are made of 24 h
15   forecasts and the meteorological fields are initialized at the beginning of each forecast with ECMWF operational analyses (Rabier et al., 2000; Janisková and Lopez, 2013). Atmospheric CO_2 is initialized on 1 January each year, using the dry molar fraction fields from the optimized fluxes provided by the MACC flux inversion system (Chevallier et al., 2011). In the subsequent forecasts, the atmospheric CO_2 is cycled from one 24 h
20   forecast to the next one, being free to evolve in the model without constraints from CO_2 observations.

  In this paper, we present results from the hindcasts with a horizontal resolution corresponding to approximately 80 km and 60 vertical levels, which is the same resolution as the current ECMWF re-analysis (ERA-Interim). This resolution is at the higher end of
25   commonly used resolutions in global Chemical Transport Models (CTM) (Belikov et al., 2013).

2.1 Transport

The modelling of the transport is performed by the IFS model operational at ECMWF. The model advection is computed by a semi-lagrangian scheme (Hortal, 2002; Untch and Hortal, 2006). Because it is not mass conserving by default, a proportional global mass fixer is used to ensure the total global budget in the model is conserved from one model time step to the next during advection. The boundary layer mixing is described in Beljaars and Viterbo (1998) and Koehler et al. (2011). The convection scheme is based on Tiedtke (1989) (see Bechtold et al., 2008, for further details). Full documentation on the IFS can be found in www.ecmwf.int/research/ifsdocs. Note that the system presented in this paper is based on model version CY38R1, which was operational from 19 June 2012 to 25 June 2013.

Results from a recent TRANSCOM model intercomparison experiment show the IFS has relatively accurate representation of the large-scale/inter-hemispheric transport, vertical profiles (Saito et al., 2013) and convective uplift (Belikov et al., 2013), with comparable skill to other CTMs participating in the TRANSCOM study, e.g. GEOSChem, PCTM and TM5. The CO_2 and SF_6 diurnal amplitudes which are largely controlled by the boundary layer mixing were also assessed by Law et al. (2008a). Their study found that the IFS was one of the models that simulated the diurnal cycles closer to those observed. Higher horizontal resolution with respect to other CTMs was found to be a contributing factor.

Finally, the NWP analysis of meteorological fields is one of the main elements determining the quality of the transport. Locatelli et al. (2013) found that methane time series simulated by IFS using ECMWF meteorological re-analysis were highly correlated to those simulated by TM5 also using the same re-analysis; whereas the average correlation of IFS with other models using different meteorological analysis was lower. Because the IFS is a world leading state-of-the-art NWP model, it is also used as a reference for the development of some CTMs, e.g. TM5 (see Krol et al., 2005).

2.2 CO$_2$ fluxes

The CO$_2$ net ecosystem exchange (NEE) fluxes are from the carbon module of the land surface model in the IFS (CTESSEL) developed as part of the Geoland project (www.gmes-geoland.info). Because the NEE fluxes are computed online, they
5 are available at the same spatial and temporal resolution as the transport model (~ 80 km resolution, every three quarters of an hour). CTESSEL is a photosynthesis-conductance (A-gs) model based on Calvet et al. (1998); Calvet (2000); Calvet et al. (2004) and developed originally by Jacobs et al. (1996). The photosynthetic fluxes are driven by radiation, soil moisture, soil temperature and a prescribed satellite MODIS
10 Leaf Area Index (LAI) monthly climatology (http://landval.gsfc.nasa.gov/). The ecosystem respiration is given by empirical formulas driven by soil moisture, soil temperature and snow cover. The meteorological forcing of the fluxes is from the NWP forecast, providing full consistency between variability of the fluxes, the meteorology and the transport processes. Because vegetation growth is represented by an LAI climatol-
15 ogy, land use change cannot be represented. There is also no direct representation of the different carbon pools, but a reference respiration parameter for each vegetation type is used to simulate the heterotrophic respiration. The reference value is obtained by optimization with respect to flux measurements for the different vegetation types. There are 9 low vegetation types and 6 high vegetation types based on the Biosphere-
20 atmosphere transfer scheme (BATS) classification (Dickinson et al., 1986). The NEE flux is an area-fraction weighted sum of the NEE for the dominant high and the dominant low vegetation classes at each grid grid-point. The evaluation of CTESSEL NEE fluxes with observations based on 10 day averaged CO$_2$ fluxes at 34 sites shows that there is an average correlation of 0.65, and an average bias and root mean square error
25 of -0.1 g C m^{-2} d^{-1} and 1.7 g C m^{-2} d^{-1} respectively. A more detailed description and evaluation of the CTESSEL Gross Primary Producion (GPP), Ecosystem respiration (R_{eco}) and the resulting NEE fluxes can be found in Boussetta et al. (2013a).

Title Page

Abstract | Introduction

Conclusions | References

Tables | Figures

|◄ | ►|

◄ | ►

Back | Close

Full Screen / Esc

Printer-friendly Version

Interactive Discussion

The fire emission flux is from GFAS v1.0 (Kaiser et al. (2012), www.copernicus-atmosphere.eu/about/project_structure/input_data/d_fire/) which is available one day behind real time. It has a daily temporal resolution and a horizontal resolution of $0.5° \times 0.5°$. The fire fluxes are kept constant throughout the 5 day forecast. The ocean sink is from the Takahashi et al. (2009) climatology with monthly mean fluxes at $4° \times 5°$ resolution. The anthropogenic fluxes are annual mean fluxes based on the last available year (2008) of the EDGAR version 4.2 inventory (edgar.jrc.ec.europa.eu). In order to account for the increase in the emissions since 2008, the growth in anthropogenic emissions beyond 2008 has been represented using a global rescaling factor. This is based on estimated anthropogenic CO_2 emission trends of −1.4 % and +5.9 % for 2009 and 2010 respectively (*Global Carbon Project*, www.globalcarbonproject.org), and a climatological trend of +3.1 % for 2011 and 2012.

3 Evaluation of CO_2 forecasts

The hindcasts have been evaluated for different periods to assess the global annual budget and its interannual variability from 2003 to 2012 (Sect. 3.1), the seasonal cycle from 2010 to 2012 (Sect. 3.2), as well as the synoptic day-to-day variability (Sect. 3.3) and diurnal cycle (Sect. 3.4). The evaluation is based on observations from the NOAA Earth System Research Laboratory (ESRL) baseline stations (www.esrl.noaa.gov/gmd/obop, Thoning et al., 2012), NOAA/ESRL tall towers (www.esrl.noaa.gov/gmd/ccgg/towers, Andrews et al., 2013), TCCON (www.tccon.caltech.edu, Wunch et al., 2011) and ICOS (www.icos-infrastructure.eu) networks. Figure 1 and Table 1 show the stations used from each network and their location. HIPPO flight data (hippo.ornl.gov/dataaccess, Wofsy et al., 2012) has also been used to evaluate CO_2 in the free troposphere (Sect. 3.5, see flight tracks in Fig. 1). Vertical profiles from the NOAA Global Monitoring Division (GMD) Carbon Cycle Vertical Profile Network (Tans et al., 1996) have been used to assess the vertical gradients in the model

from the lower to the mid troposphere. The computations involved in the processing of the CO_2 hindcast for the comparison with observations are described in the Appendix.

3.1 Global CO_2 budget and its interannual variability

The model atmospheric CO_2 growth is the result of the addition of all the fluxes shown in Fig. 2a. Because the model is not constrained by CO_2 observations, the budget of the total emissions does not match the observed atmospheric growth. This leads to an annual global bias in the modelled CO_2. In the case of optimized fluxes, there is a reasonably good fit between their budget and the observed global growth. Hence, they can be used as a reference, representing a current best estimate for the fluxes.

The annual bias of the model varies from year to year because there are two compensating errors opposing each other. Namely, the underestimation of the NEE sink in Northern Hemisphere (NH) summer and the underestimation of NEE release in NH winter by 1 to $2\,\mathrm{Gt\,C\,month^{-1}}$ (Fig. 2b) compared to the optimized fluxes of Chevallier et al. (2011). Therefore, the sign of the resulting annual global bias depends on which of these errors dominates when integrated over the year. For instance, in 2010 and 2011 the underestimation of the NEE source is larger than the underestimation of the sink, resulting in a negative global annual bias. Whereas in 2012 the opposite occurs, the underestimation of the sink is larger than that of the source, thus the positive annual global bias. The interannual variability of atmosperic growth is modulated by the NEE interannual variability.

The correlation between the modelled and observed global annual atmospheric growth is 0.74. Although the main contributor to the annual NEE global sink is the NH, the tropics are responsible for its large interannual variability (Fig. 2c).

The strong seasonal cycle in the global atmospheric growth (see grey curve in Fig. 2b, defined as the sum of all the surface flux components) comes mainly from the NH mid-latitudes between 30° N and 66° N (Fig. 2d). This suggests that the large underestimation of the global seasonal cycle amplitude is likely associated with errors

in midlatitude NEE fluxes. The errors associated with the modelling of the seasonal cycle are examined further in the next section.

3.2 CO_2 seasonal cycle

The phase and amplitude of the seasonal cycle of CO_2 are very dependent on latitude. Thus, the model is first evaluated using the NOAA GLOBALVIEW-CO2 (2011) dataset which displays the integrated effects of surface CO_2 fluxes over large regions at different latitudinal bands (Fig. 3). At first glance, the annual cycle phase and amplitude and latitude dependency appears to be reasonably represented in the hindcast. However, there are clear discrepancies between the hindcast and GLOBALVIEW-CO2 (2011) in the NH. First of all, the hindcast does not release enough CO_2 before and after the growing season (i.e. March to May and October to December). Secondly, the onset of the CO_2 sink associated with the growing season starts too early in the hindcast. The sharp CO_2 decrease in mid-latitudes depicted by GLOBALVIEW-CO2 (2011) in June starts in May in the hindcast. This also leads to a longer growing season. The combination of these two factors is consistent with the negative global bias shown in Fig. 2. The GLOBALVIEW-CO2 (2011) evaluation is corroborated by comparison with continuous measurements of background air from the NOAA/ESRL network, total column measurements from the TCCON network and continuous measurements from the ICOS network. Figure 1 shows the location of the observing stations.

The monthly biases at three continuous ESRL/NOAA background sites (Thoning et al., 2012) confirm that the largest biases are in the NH, as shown by the -10 ppm to -5 ppm bias in the summer months at Barrow, Alaska (Fig. 4a). The negative bias increases in the NH growing season from March to June. This is shown by the differential monthly bias, which depicts how the bias changes with respect to the previous month. The stations in the tropics and South Pole also display mainly negative monthly biases in the background air, with smaller magnitudes, typically between -1 and -2 ppm. Every year, the hindcast is re-initialized with fields from optimized flux simulations constrained with CO_2 observations that convey the atmospheric growth.

The differential bias in January each year, thus, depicts the adjustment applied in order to correct for the annual global mean bias in the previous year (see blue dots in Fig. 4). The annual bias in the tropics and South Pole sites is consistent with the bias of the global budget shown in Fig. 2a. The largest interannual variability in the annual bias is also found for the tropical sites. This variability is consistent with that of the bias in the annual global budget. The anomalous 2005 positive annual biases of 1.5 and 2 ppm at the tropical and South Pole sites respectively are in line with the 2.5 Gt C annual global bias (equivalent to 1.2 ppm).

The results from the total column evaluation (Fig. 5) are consistent with the findings from the surface measurements and GLOBALVIEW comparisons (Figs. 4 and 3). In Sodankylä (Finland) and Bialystok (Poland) we observe the same underestimation of column CO_2 during NH winter. The hindcast also brings forward the onset of the CO_2 drawdown associated with the growing season by a month. Namely, the observed steep total column CO_2 decrease in June at Sodankylä starts in early May in the model. Similarly, at Bialystok the beginning of the observed CO_2 drawdown is May, whereas the modelled total column CO_2 starts decreasing in April. At Parkfalls (Winsconsin, USA) total column CO_2 is underestimated before and after the summertime CO_2 drawdown, and at Lamont (Oklahoma, USA) the CO_2 is only underestimated in winter (January, November and December).

The evaluation of the seasonal cycle based on the ICOS stations (Fig. 6) is similarly in agreement with previous findings. Ivittut (Greenland) and Puijo (Finland) confirm the underestimation of the winter CO_2 respiration, and the negative bias in Mace Head (Ireland) is also consistent with an underestimation of CO_2 which starts in winter and becomes more pronounced in spring. The CO_2 spikes in Mace Head are associated with specific events influenced by local and nearby continental sources/sinks (Biraud et al., 2002). The background stations of Ivittut and Mace Head have a negative annual bias of ~ -3 ppm whereas Puijo which is affected by local vegetation fluxes has an annual bias of ~ -5 ppm. Finally, Lamto (Ivory coast) shows a large positive bias during the dry season when the site is influenced by continental biogenic fluxes, and a small

Title Page

Abstract | Introduction

Conclusions | References

Tables | Figures

|◄ | ►|

◄ | ►

Back | Close

Full Screen / Esc

Printer-friendly Version

Interactive Discussion

bias during the wet season when the monsoon winds advect background CO_2 from the ocean.

3.3 CO_2 synoptic variability

An evaluation of the variability associated with synoptic events is performed at three tall tower sites of the NOAA/ESRL network in continental North America (Argyle, Park Falls and West Branch, see Andrews et al., 2013). These sites are directly influenced by local land biospheric fluxes, atmospheric transport and their interaction. The skill in representing the day-to-day variability is assessed for different months in Sect. 3.3.1 and the importance of modelling NEE for the synoptic skill is assessed in Sect. 3.3.2.

3.3.1 Forecast skill of day-to-day CO_2 variability

The synoptic variability is evaluated first by computing the correlation between daily mean atmospheric CO_2 from observations and hindcasts (Table 2) at different sampling levels (Table 3). The correlation coefficients are predominantly higher than 0.5 in the winter months – January, February, November and December – and most sites have values between 0.65 and 0.95. Most of the variability is linked to low pressure systems advecting CO_2 across the large-scale meridional gradient, with a small modulation associated with biogenic fluxes indicated by the very low correlations between atmospheric CO_2 and the modelled NEE fluxes (not shown). In general, the CO_2 hindcast is able to accurately represent the variability associated with the advection by synoptic weather systems.

The spring months – from March to May – display very low or not significant correlations. The large errors in spring (both poor correlations and large biases) are likely associated with modelling errors in the GPP and R_{eco}. Spring is a challenging period for carbon models to model NEE because it is characterized by the transition from predominant respiration in winter to predominant photosynthetic uptake. The timing of this shift in the sign of the daily mean NEE has been analyzed in the model at the

two sites where the correlation coefficients are lowest (Park Falls and West Branch). In the model the transition occurs at the beginning of March, which is consistent with the concurrent underestimation of the modelled atmospheric CO_2 and the early onset of the CO_2 drawdown season shown in Sect. 3.2.

In the summer months, correlation coefficients are mostly above 0.5, with slightly lower values at Argyle, Maine. During summer, the local fluxes and local transport (e.g. the height of the nocturnal boundary layer) have a large influence on the synoptic variability, which is reflected by the higher correlations between atmospheric CO_2 and those parameters (not shown). Local circulations, nocturnal stable boundary layers and the high vegetation activity in the summer are all associated with high uncertainties in the model. The correlations are lower due to the combined effect of the large uncertainties in these local influences.

In autumn, the correlations are higher than in summer. From September to November, both synoptic transport by mid-latitude low pressure systems and biogenic fluxes are important. Moreover, the coupling between the transport and the fluxes is crucial. This is illustrated in Fig. 7 showing the day-to-day variability in tower in situ data from Park Falls in September 2010. The model is able to simulate the peaks of CO_2 on the 7, 11, 21, 23–24 and 29 September 2010, all of them associated with the passage of low pressure systems. The correlation coefficient between observed and modelled CO_2 is 0.81. The modelled and observed CO_2 are similarly correlated with surface pressure (correlation coefficient $r = -0.52$ and $r = -0.56$ respectively) and NEE ($r = 0.58$ and $r = 0.57$ respectively).

3.3.2 Impact of NEE day-to-day variability on the atmospheric CO_2 synoptic forecast skill

The relative importance of the synoptic variability of NEE vs. transport can be assessed by comparing the standard hindcast with a simulation using 3 hourly monthly mean NEE from CTESSEL (i.e. without day-to-day variability) instead of real-time NEE. Figure 8 shows the day-to-day variability of daily minimum, maximum and mean CO_2

at 30 m and 396 m level above the surface from the tall tower at Park Falls for the two simulations and observations in September 2010. The observed CO_2 variability is characterized by a trend associated with the seasonal cycle and day-to-day synoptic variability. The variability of the minimum CO_2 during day time is dominated by the trend. Whereas at night time, the CO_2 maximum is modulated by synoptic variations. As expected, the CO_2 day-time trend is present in the hindcast with real-time NEE, but absent in the simulation with the monthly mean NEE. The underestimation of the trend in the hindcast with real-time NEE is consistent with the biases in the seasonal cycle (see Sect. 3.2).

The observed synoptic variability is always larger than in the hindcast. By using monthly mean NEE the simulated variability is further dampened. This suggests that although the transport plays a first order role in the synoptic variability of atmospheric CO_2, the day-to-day variability of NEE also plays an important role in enhancing it. This is confirmed in Table 4 where the correlations between the detrended CO_2 from the model and observations at the two levels of the tall tower at Park Falls are shown for the two simulations with and without NEE day-to-day variability. The simulated CO_2 always correlates better with observations when the synoptic variability of NEE is included, except when the observations are sampling the free troposphere. That is the case for the 396 m level during nighttime, when large-scale advection dominates the variability and both simulations have very high correlations coefficients.

The passage of frontal low pressure systems is responsible for the long-range transport of CO_2 via their warm conveyor belts which lift CO_2 rich air from the surface to the mid and upper-troposphere. This large-scale advection is illustrated in Fig. 9 where positive CO_2 anomalies originating from the surface are shown in the region of frontal ascent at different vertical levels (850, 500 and 300 hPa). On 21 and 23–24 September, Park Falls experiences the advection of positive CO_2 anomalies associated with the passage of two different low pressure systems.

The cloudy warm conveyor belts in the mid-latitude low pressure systems are also associated with changes in temperature and solar radiation at the surface which in

Title Page

Abstract | Introduction

Conclusions | References

Tables | Figures

|◄ | ►|

◄ | ►

Back | Close

Full Screen / Esc

Printer-friendly Version

Interactive Discussion

turn produce an increase in NEE (Fig. 7). This increase in NEE can be associated with a decrease in GPP following a decrease in radiation (e.g. 3 and 7 September), an increase in R_{eco} following an increase in temperature (e.g. 21 September), or both a simultaneous decrease in GPP and increase in R_{eco} due to a concurrent decrease in radiation and increase in temperature (e.g. 11 and 23–24 September). It is also interesting to note that on 29 September, the passage of a low pressure system lead to an increase in temperature at Park Falls, resulting in a simultaneous increase in GPP and R_{eco}. In the model the increase in GPP is larger than the increase in R_{eco}, leading to a decrease in NEE. This NEE decrease opposes the observed increase in atmospheric CO_2.

3.4 CO_2 diurnal cycle

The diurnal cycle is assessed at two ICOS sites, one in Europe (Cabauw, the Netherlands) and one in Africa (Lamto, Ivory Coast). The amplitude of the diurnal cycle varies strongly at synoptic scales as shown by Figs. 10 and 12. This variability affects mainly the higher-values of CO_2 at nighttime, whereas the daytime CO_2 has a much lower monthly standard deviation (Fig. 11). As expected, the amplitude of the diurnal cycle decreases rapidly with height at the ICOS tall tower at Cabauw, Netherlands. The CO_2 hindcast is able to reproduce the changes in the amplitude of the diurnal cycle, both in time and in height. At the lower level (20 m), the model overestimates the variability of the nocturnal CO_2 values by largely overestimating the CO_2 peaks during three specific nights (24–25, 26–27 and 27–28 September). These are days when the 10 m wind speed drops to $1\,\mathrm{m\,s^{-1}}$ and the boundary layer height is very shallow. Under these conditions the CO_2 hindcast is highly uncertain because of both uncertainties in the mixing under stable conditions (Sandu et al., 2013) and the strong influence of the errors in the surface fluxes when the boundary layer collapses. In the hindcast, the daytime CO_2 trough is consistently underestimated at all vertical levels, which is consistent with the negative global bias described in Sects. 3.1 and 3.2.

At the tropical African site of Lamto, Ivory Coast, the diurnal cycle also shows the largest errors are at nighttime with an overestimation of CO_2 (Fig. 12), which is consistent with the positive bias in the CO_2 hindcast during the dry season. Nevertheless, it is clear that the nighttime overestimation does not occur every day (Fig. 12a). This suggests there is a variable forcing responsible for the errors associated with the CO_2 hindcast.

Correlations of the daily mean CO_2 with both boundary layer height and NEE fluxes from the model have been computed, in order to find which one is the main driver in the synoptic variability of the diurnal cycle amplitude. The daily mean boundary layer height from the model correlates well with the observed and modelled diurnal cycle amplitude of CO_2 at Cabauw with a correlation coefficient of -0.73 for the two of them. Both nighttime and daytime boundary layer heights play a role in the synoptic variability of diurnal cycle at Cabauw. At Lamto the most important factor explaining the synoptic variability of the diurnal cycle amplitude is the nighttime boundary layer height, with correlation values of -0.50 and -0.67 for the observed and modelled amplitude of the CO_2 diurnal cycle respectively. The correlation of the daily mean CO_2 and the NEE fluxes is below 0.3 at both sites. This implies that the NEE fluxes alone are not able to explain the synoptic variability of the diurnal cycle at those sites in September 2011. Although the boundary layer height at both Cabauw and Lamto appears to be the main factor explaining the variability of the diurnal cycle amplitude, this does not mean that the surface fluxes do not contribute. In fact, this evaluation shows that the surface fluxes and their errors have their effect enhanced under very stable conditions, when the boundary layer is very shallow.

3.5 Interhemispheric gradient of CO_2

The interhemispheric gradient of CO_2 has been evaluated using the HIPPO flight campaign data (Wofsy, 2011; Wofsy et al., 2012) in 2010 and 2011 (Fig. 13). In order to compare the simulated and observed CO_2, the model data closest to the observed data in time and space is used. In March and April the comparison shows that the CO_2-rich

outflow from Asia in the region of the subropical jet is overestimated in the simulations. Background biases fall between −1 and −4 ppm, except for the mid and high latitudes where the background biases range between −8 and −4 ppm. These are consistent with the monthly biases in the seasonal cycle of surface and total column stations pre-sented in Sect. 3.2. As a result of this negative bias in the lower mid-troposphere at NH mid-latitudes, the interhemispheric gradient is too strong in the summer and too weak in the spring. Similarly the negative vertical gradient between the lower and upper-troposphere in spring is too weak and the positive vertical gradient in the summer is too strong.

3.6 Vertical gradient of CO₂

One of the most important and more uncertain parts of the transport is the vertical mixing and the resulting vertical profiles over continental regions with strong surface fluxes (Kretschmer et al., 2012). There is a large variability between models in the simulation of vertical gradients and this strongly affects their consensus in the optimized NEE fluxes derived from different flux inversion systems (Stephens et al., 2007). In order to assess the performace of the hindcast in representing the vertical profiles, the model has been compared with observed vertical profiles at midday from NOAA/ESRL aircraft data in North America (Fig. 14a), following Stephens et al. (2007).

Results show an underestimation of the vertical gradient in both the lower and mid troposphere during winter (Fig. 14b–d). The observed difference in the lower tropo-sphere between altitudes of 1 and 4 km is +2.26 ppm compared to the modelled dif-ference of +1.10 ppm. In the mid troposphere the discrepancy is smaller, +0.99 ppm between 4 and 6 km in the observations vs. +0.78 ppm in the model. The gradient is reversed and less steep during the summer. This is due to the change of sign in the NEE flux – from net release in winter to net uptake in summer – as well as the stronger vertical mixing associated with more convectively unstable atmospheric conditions. The model is able to simulate these changes, but still underestimates the observed gradient of −0.86 ppm in the lower troposphere compared to −0.47 ppm in the model.

4 Discussion

The hindcast performance is discussed in this section and possible ways of improving its deficiencies are described. The errors in the simulated CO_2 are dominated by errors in the fluxes. This is shown by the errors in the global budget, correlation coefficients and consistent biases computed using flight vertical profiles, total column observations as well as surface observations.

The largest biases are in the NH, particularly in the Arctic region (north of 66° N). However, this does not imply that the error in the fluxes is largest there. It is very likely that the larger negative biases in the arctic reflect the fact that the CO_2 biases from NH mid-latitudes (defined here between 30° N and 66° N) are transported northwards, consistently with the amplification of seasonal cycle in the arctic due to the coupling between mid-latitude fluxes and transport as described by Parazoo et al. (2011). The flux signal in the NH is coming predominantly from mid-latitudes, which include the boreal forests. Keppel-Aleks et al. (2011) demonstrated that small errors in NEE fluxes in the boreal region between 45 and 65° N have a larger impact on the seasonal cycle amplitude of total column atmospheric CO_2 than changes at lower latitudes, due to the greater seasonality of NEE in the boreal region.

NH Spring is the season where the largest errors occur, both in budget (bias) and in the synoptic variability (correlations). Other models also found the spring months to have the lowest correlation coefficients with observed daily CO_2 (e.g. Geels et al., 2004; Pillai et al., 2011). This is not surprising as the onset of the CO_2 drawdown associated with the growing season causes a rapid shift in the dominant component of the NEE, i.e. from R_{eco} to GPP. The simulated biogenic fluxes experience this shift in early spring (March) for two sites associated with cold temperate deciduous forest and corn crops; whereas in reality this shift occurs later on between April and May (see Fig. 8 of Falge et al., 2002). The intercomparison of several modelled NEE datasets with TCCON observations by Messerschmidt et al. (2013) showed that the best fit with the TCCON data was given by the SiB model which had the 20–75° N aggregated NEE shift in

April. The reasons for the one month error in the start of the growing season need to be further investigated. Possible candidates are the representation of the sensitivities of R_{eco} and GPP to the variations of temperature and radiation in the CTESSEL model (Balzarolo et al., 2013), and the uncertainties associated with the estimation of the reference respiration as well as the simplistic radiative transfer scheme for vegetation (Boussetta et al., 2013a).

Other seasons show much larger correlation coefficients, particularly in the NH winter and autumn where the variability is explained by the coupling between meteorology (i.e. transport) and flux variability associated with the passage of frontal low pressure systems. The correlation coefficients at the tall towers which are influenced by vegetation are higher than those presented so far by other models with similar or higher horizontal resolution (Geels et al., 2004; Pillai et al., 2011). This is very encouraging and it emphasizes the importance of the interaction between meteorological transport and forcing of the fluxes in the simulation of the CO$_2$ synoptic variability. The NEE synoptic variability plays an important role at enhancing this CO$_2$ day-to-day variability. Within the boundary layer this effect is even more important, as the local fluxes play a more prominent role in modulating the atmospheric concentrations. In other words, the synoptic variability of atmospheric CO$_2$ could not be properly represented using climatological CO$_2$ fluxes, or offline biogenic CO$_2$ fluxes forced by climatologies of meteorological fields.

The sign of the vertical gradient is well represented in the hindcast, but the magnitude of the gradient is underestimated in the lower troposphere, particularly during winter. Although the fluxes can also be responsible for this underestimation, it is very likely that the vertical diffusion in the model is also contributing by having too much vertical mixing. This is a well-known problem in NWP models – including the IFS – which enhance the turbulent diffusion in stable conditions in order to compensate for errors caused by other poorly represented processes, such as orographic drag and the strength of the land–atmosphere coupling (Sandu et al., 2013).

The evaluation of the diurnal cycle also confirms that the boundary layer height and the 10 m wind speed are important controlling factors on the large day-to-day variability in the skill of the CO_2 hindcast. Under stable conditions when the boundary layer is shallower, there is an enhanced impact of the surface flux and their associated errors on the atmospheric CO_2 close to the surface. At the same time, the errors associated with turbulent mixing are also largest in stable conditions (Sandu et al., 2013).

5   Summary and further developments

This paper documents a new CO_2 forecast product from the MACC-II project, the pre-operational Copernicus atmospheric service. The CO_2 hindcast skill has been assessed at global to local scales and at temporal scales ranging from interannual variability to the diurnal cycle using a wide range of observations. Overall the hindcast can simulate very well the CO_2 synoptic variability modulated by the coupling between meteorological forcing of the fluxes and transport. Comparing the synoptic variability with and without day-to-day variability in NEE indicates that in order to improve the synoptic skill of a CO_2 forecast, it is imperative to include and improve the day-to-day variability of the NEE fluxes, as well as its large-scale gradient. Improvements in the modelling of CO_2 fluxes and transport are expected as part of the ongoing efforts to upgrade the real-time CO_2 forecasting system of the Copernicus atmospheric service, in line with the updates of the operational IFS at ECMWF. For instance, the new developments in the convection and vertical diffusion parameterizations (Bechtold et al., 2014; Sandu et al., 2013) have been shown to have a positive impact on the diurnal cycle of convection and near-surface winds in the new IFS model cycle CY40R1. These improvements in the transport are also expected to lead to improvements in the CO_2 forecast. There are also developments in the assimilation of new satellite products in the IFS that could have a significant impact on the modelling of the CO_2 fluxes. For example, the near-real time albedo and LAI from the Copernicus Global Land Service (Boussetta et al., 2014), and the SMOS/ASCAT soil moisture products (Muñoz-Sabater

et al., 2012, 2013; de Rosnay et al., 2012) could improve the phenology and the meteorological forcing on the modelled NEE fluxes respectively. Further improvements of the vegetation radiative transfer scheme based on Carrer et al. (2013) are also planned for the near future.

Currently, the forecast is not constrained by CO_2 observations. Thus, there is an accumulating global bias (ranging from 2 to 4 ppm in magnitude). The bias is largest in the NH and it is associated predominantly with errors in the NEE fluxes in NH midlatitudes, particularly during the growing season in spring. This model bias is larger than the bias of the currently available satellite CO_2 retrievals from GOSAT (www.gosat.nies.go.jp) of only a few tenths of ppm (Notholt et al., 2013). Therefore, when such retrievals can be assimilated in near-real time in order to produce a CO_2 analysis to initialize the CO_2 forecast with, the bias of the forecast will also be reduced. Because the CO_2 forecast has good skill in simulating the synoptic variability of CO_2 in real time, it should provide a good background state for the assimilation of the available CO_2 observations and satellite retrievals from GOSAT, as well as other upcoming satellite missions, e.g. OCO-2 (oco.jpl.nasa.gov).

The CO_2 observations provided in near-real time by the operational ICOS network are invaluable for the necessary CO_2 forecast error assessment. Continuous monitoring of the MACC-II CO_2 forecast based on the operational ICOS network is available online one day behind real time (www.copernicus-atmosphere.eu/d/services/gac/verif/ghg/icos).

The CO_2 forecast presented in this paper aims at providing information on the spatial and temporal variations of atmospheric CO_2 in real time. As such, it can be useful for a variety of purposes. For example, the atmospheric CO_2 fields can provide a link to collocate the CO_2 retrievals from satellite observations in time and spatial with ground-based observations for calibration, bias correction and evaluation purposes (Notholt et al., 2011). Some satellite retrievals also rely on model-based CO_2 products to infer methane total columns and therefore avoid the expensive simulation of radiative scattering (Frankenberg et al., 2011). Other uses include the provision of

boundary conditions for regional modelling and flux inversions (Matross et al., 2006; Rivier et al., 2010; Schuh et al., 2010; Broquet et al., 2011), helping the interpretation of observations (Schneising et al., 2012) and supporting the planning of field experiments (Carmichael et al., 2003). Finally, having real time estimates for atmospheric CO_2 abundances has also other potential benefits, including a better representation of the model radiation and the radiance observation operator (Bechtold et al., 2009; Engelen and Bauer, 2011), as well as evapotranspiration (Boussetta et al., 2013b) in NWP analyses and forecasts.

The real-time global CO_2 forecast is now part of the MACC-II suite of products freely available from the MACC-II data catalogue (www.copernicus-atmosphere.eu/catalogue).

Appendix A: Comparing model with observations

Before comparing the model with observations, the atmospheric CO_2 modelled fields need to be processed in order to match the modelled with the observed quantities, including a collocation in space and time. The first step is to extract the vertical profile from the 3 hourly archived CO_2 forecast fields at the nearest land gridpoint to the location of the observation. For in situ observations, a linear interpolation to the observation height above the surface is performed in altitude. The last step is to collocate the observation and model in time. This is done by linearly interpolating the forecast data in time to match the observation time. The specific computations for the in situ (including the NOAA/ESRL flights) and total column observations are described below.

A1 In situ observations

In order to interpolate the model data to the sampling height for the in situ observations, at each grid point the pressure of the model layer boundaries p_l is converted to altitude

z_l^h by:

$$z_l^h = z_{l+1}^h + \frac{R_d}{g} T_l (1.0 + 0.61 q_l) \ln\left(\frac{p_{l+1}}{p_l}\right), \tag{A1}$$

where $R_d = 287.06$, $g = 9.8066$ and l ranges from 1 to NLEV+1 with $z_{NLEV+1}^h = 0$. Then the elevation in the middle of the model layer z is computed for each level i ranging from 1 to NLEV by:

$$z_i = \frac{z_{i+1}^h + z_i^h}{2} \tag{A2}$$

A2 TCCON observations

The TCCON retrieved total columns are directly compared to the integrated averaging kernel-smoothed profile derived from the model CO_2 dry molar fraction profile (x_m) following Rodgers and Connor (2003) and Wunch et al. (2010):

$$c_s = c_a + \boldsymbol{h}^T \boldsymbol{a}^T (\boldsymbol{x}_m - \boldsymbol{x}_a) \tag{A3}$$

where c_s is the smoothed model forecast column average, c_a is the a priori total column, $\boldsymbol{a}$ is a vector containing the TCCON absorber-weighted column averaging kernel, $\boldsymbol{h}^T$ is a dry-pressure weighting function, and $\boldsymbol{x}_a$ is the a priori CO_2 dry molar fraction profile.

All the quantities of Eq.(A3) are interpolated onto the same model vertical grid. As the IFS has a hybrid-sigma pressure vertical grid, the model levels have corresponding pressure levels that vary in space and time.

The number of model levels (NLEV) used by the model forecast in this paper is 60. Note that the model does not provide any CO_2 dry molar fraction value at the surface. The model vertical levels are bounded by NLEV+1 half pressure levels (from 0 Pa to the surface pressure).

Eq. (A3) can be re-written as

$$c_s = c_a + \left(c_m^{ak} - c_a^{ak} \right).$$ (A4)

where c_m^{ak} and c_a^{ak} are the averaging kernel-weighted dry-pressure-weighted vertical columns from the model and a priori profiles respectively. The three terms are computed as the sum over each pressure level i:

$$c_a = \sum_{i=0}^{NLEV} \overline{(x_a)_i} \, \tilde{h}_i,$$ (A5)

$$c_m^{ak} = \sum_{i=0}^{NLEV} \overline{(x.a)_i} \, \tilde{h}_i, \text{ and } c_a^{ak} = \sum_{i=0}^{NLEV} \overline{(x_a.a)_i} \, \tilde{h}_i,$$ (A6)

Note that $\tilde{h}$ is an approximation of the dry-pressure weighted function following O'Dell et al. (2012) given by:

$$\tilde{h}_i = \frac{\overline{c_i} \, \Delta p_i}{\sum_{i=0}^{NLEV} \overline{c_i} \, \Delta p_i},$$ (A7)

with

$$c_i = \frac{(1 - q_i)}{g_i \, M_{air}^{dry}},$$ (A8)

where q_i and g_i are the specific humidity and the gravitational acceleration at pressure level i ($q_i = q(p_i)$, $g_i = g(p_i)$), and M_{air}^{dry} is the molar mass of dry air. The bar denotes the average over a pressure layer computed as

$$\overline{c_i} = \frac{c_{i+1} + c_i}{2}$$ (A9)

$$\overline{(x_m.a)_i} = \frac{(x_m a)_{i+i} + (x_m a)_i}{2}$$ (A10)

13933

with $\overline{(x_m.a)_0} = \frac{(x_m a)_1}{2}$ and $\overline{(x_m.a)}_{NLEV} = (x_m a)_{NLEV}$.

$$\overline{(x_a)}_i = \frac{(x_a)_{i+i} + (x_a)_i}{2} \tag{A11}$$

and

$$\overline{(x_a.a)}_i = \frac{(x_a a)_{i+i} + (x_a a)_i}{2} . \tag{A12}$$

The boundary conditions are $\overline{(x_a)_0} = \frac{(x_a)_1}{2}$, $\overline{(x_a.a)_0} = \frac{(x_a a)_1}{2}$, $\overline{(x_a)}_{NLEV} = (x_a)_{NLEV}$ and $\overline{(x_a.a)}_{NLEV} = (x_a a)_{NLEV}$.

References

Andrews, A. E., Kofler, J. D., Trudeau, M. E., Williams, J. C., Neff, D. H., Masarie, K. A., Chao, D. Y., Kitzis, D. R., Novelli, P. C., Zhao, C. L., Dlugokencky, E. J., Lang, P. M., Crotwell, M. J., Fischer, M. L., Parker, M. J., Lee, J. T., Baumann, D. D., Desai, A. R., Stanier, C. O., de Wekker, S. F. J., Wolfe, D. E., Munger, J. W., and Tans, P. P.: CO_2, CO and CH_4 measurements from the NOAA Earth System Research Laboratory's Tall Tower Greenhouse Gas Observing Network: instrumentation, uncertainty analysis and recommendations for future high-accuracy greenhouse gas monitoring efforts, Atmos. Meas. Tech. Discuss., 6, 1461–1553, doi:10.5194/amtd-6-1461-2013, 2013. 13917, 13921

Balzarolo, M., Boussetta, S., Balsamo, G., Beljaars, A., Maignan, F., Calvet, J.-C., Lafont, S., Barbu, A., Poulter, B., Chevallier, F., Szczypta, C., and Papale, D.: Evaluating the potential of large scale simulations to predict carbon fluxes of terrestrial ecosystems over a European Eddy Covariance network, Biogeosciences Discuss., 10, 11857–11897, doi:10.5194/bgd-10-11857-2013, 2013. 13928

Bechtold, P., Köhler, M., Jung, T., Doblas-Reyes, F., Leutbecher, M., Rodwell, M., Vitart, F., and Balsamo, G.: Advances in simulating atmospheric variability with the ECMWF model: from synoptic to decadal time-scales, Q. J. Roy. Meteor. Soc., 134, 1337–1351, 2008. 13915

Bechtold, P., Orr, A., Morcrette, J.-J., Engelen, R., Flemming, J., and Janiskova, M.: Improvements in the stratosphere and mesosphere of the IFS, Newsletter 120, ECMWF, Reading, Berkshire, UK, 2009. 13931

Bechtold, P., Semane, N., Lopez, P., Chaboureau, J.-P., Beljaars, A., and Bormann, N.: Representing equilibrium and nonequilibrium convection in large-scale models, J. Atmos. Sci., 71, 734–753, 2014. 13929

Belikov, D. A., Maksyutov, S., Krol, M., Fraser, A., Rigby, M., Bian, H., Agusti-Panareda, A., Bergmann, D., Bousquet, P., Cameron-Smith, P., Chipperfield, M. P., Fortems-Cheiney, A.,

Title Page

Abstract | Introduction

Conclusions | References

Tables | Figures

|◄ | ►|

◄ | ►

Back | Close

Full Screen / Esc

Printer-friendly Version

Interactive Discussion

Gloor, E., Haynes, K., Hess, P., Houweling, S., Kawa, S. R., Law, R. M., Loh, Z., Meng, L., Palmer, P. I., Patra, P. K., Prinn, R. G., Saito, R., and Wilson, C.: Off-line algorithm for calculation of vertical tracer transport in the troposphere due to deep convection, Atmos. Chem. Phys., 13, 1093–1114, doi:10.5194/acp-13-1093-2013, 2013. 13914, 13915

5   Beljaars, A. and Viterbo, P.: The role of the boundary layer in a numerical weather prediction model, in: Clear and Cloudy Boundary Layers, Royal Netherlands Academy of Arts and Sciences, North Holland Publishers, Amsterdam, 1998. 13915

Biraud, S., Ciais, P., Ramonet, M., Simmonds, P., Kazan, V., Monfray, P., O'Doherty, S., Spain, G., and Jennings, G.: Quantification of carbon dioxide, methane, nitrous oxide and

10   chloroform emissions over Ireland from atmospheric observations at Mace Head, Tellus B, 54, 41–60, 2002. 13920

Boussetta, S., Balsamo, G., Beljaars, A., Agusti-Panareda, A., Calvet, J.-C., Jacobs, C., van den Hurk, B., Viterbo, P., Lafont, S., Dutra, E., Jarlan, L., Balzarolo, M., Papale, D., and van der Werf, G.: Natural carbon dioxide exchanges in the ECMWF Integrated Fore-

15   casting System: implementation and offline validation, J. Geophys. Res.-Atmos., 118, 1–24, doi:10.1002/jgrd.50488, 2013a. 13911, 13916, 13928

Boussetta, S., Balsamo, G., Beljaars, A., and Jarlan, J.: Impact of a satellite-derived Leaf Area Index monthly climatology in a global Numerical Weather Prediction model, Int. J. Remote Sens., 34, 3520–3542, 2013b. 13931

20   Boussetta, S., Balsamo, G., Beljaars, A., and Dutra, E.: Monitoring vegetation with satellite observations products (LAI and Albedo) assimilated in the ECMWF modelling, in: Global Vegetation Monitoring and Modeling International Conference, Avignon, France, available at: https://colloque.inra.fr/gv2m/Oral-Sessions (last access: 20 May 2014), 2014. 13929

Broquet, G., Chevallier, F., Rayner, P., Aulagnier, C., Pison, I., Ramonet, M., Schmidt, M.,

25   Vermeulen, A., and Ciais, P.: A European summertime CO_2 biogenic flux inversion at mesoscale from continuous in situ mixing ratio measurements, J. Geophys. Res., 116, D23303, doi:10.1029/2011JD016202, 2011. 13931

Calvet, J.-C.: Investigating soil and atmospheric plant water stress using physiological and micrometeorological data, Agr. Forest Meteorol., 103, 229–247, 2000. 13916

30   Calvet, J.-C., Noilhan, J., Roujean, J.-L., Bessemoulin, P., Cabelguenne, M., Olioso, A., and Wigneron, J.-P.: An interactive vegetation SVAT model tested against data from six contrasting sites, Agr. Forest Meteorol., 92, 73–95, 1998. 13916

Calvet, J.-C., Rivalland, V., Picon-Cochard, C., and Guehl, J. M.: Modelling forest transpiration and CO_2 fluxes – Response to soil moisture stress, Agr. Forest Meteorol., 124, 143–156, 2004. 13916

Carmichael, G., Tang, Y., Kurata, G., Uno, I., Streets, D., Woo, J.-H., Huang, H., Yienger, J., Lefer, B., Shetter, R., Blake, D., Atlas, E., Fried, A., Apel, E., Eisele, F., Cantrell, C., Avery, M., Barrick, J., Sachse, G., Brune, W., Sandholm, S., Kondo, Y., Singh, H., Talbot, R., Bandy, A., Thorton, D., Clarke, A., and Heikes, B.: Regional-scale chemical transport modeling in support of the analysis of observations obtained during the TRACE-P experiment, J. Geophys. Res., 108, 1–44, doi:10.1029/2002JD003117, 2003. 13931

Carrer, D., Roujean, J. L., Lafont, S., Calvet, J.-C., Boone, A., Decharme, B., Delire, C., and Gastellu-Etchegorry, J.-P.: A canopy radiative transfer scheme with explicit FAPAR for the interactive vegetation model ISBA-A-gs: Impact on carbon fluxes, J. Geophys. Res., 118, 888–903, doi:10.1002/jgrg.20070, 2013. 13930

Chan, D., Yuen, C., Higuchi, K., Shashkov, A., Liu, J., Chen, J., and Worthy, D.: On the CO_2 exchange between the atmosphere and the biosphere: the role of synoptic and mesoscale processes, Tellus B, 56, 194–212, 2004. 13912

Chevallier, F., Deutscher, N., Conway, T., Ciais, P., Ciattaglia, L., Dohe, S., Fröhlich, M., Gomez-Pelaez, A., Griffith, D., Hase, F., Haszpra, L., Krummel, P., Kyrö, E., Labuschne, C., Langenfelds, R., Machida, T., Maignan, F., Matsueda, H., Morino, I., Notholt, J., Ramonet, M., Sawa, Y., Schmidt, M., Sherlock, V., Steele, P., Strong, K., Sussmann, R., Wennberg, P., Wofsy, S., Worthy, D., Wunch, D., and Zimnoch, M.: Global CO_2 fluxes inferred from surface air-sample measurements and from TCCON retrievals of the CO_2 total column, Geophys. Res. Lett., 38, L24810, doi:10.1029/2011GL049899, 2011. 13914, 13918, 13950

de Rosnay, P., Drusch, M., Vasiljevic, D., Balsamo, G., Albergel, C., and Isaksen, L.: A simplified Extended Kalman Filter for the global operational soil moisture analysis at ECMWF, Q. J. Roy. Meteor. Soc., 139, 1199–1213, doi:10.1002/qj.2023, 2012. 13930

Denning, A., Takahashi, T., and Friedlingstein, P.: Can a strong atmospheric CO_2 rectifier effect be reconciled with a "reasonable" carbon budget?, Tellus B, 51, 249–253, 1999. 13913

Dickinson, R., Henderson-Sellers, A., Kennedy, P., and Wilson, M. F.: Biosphere-atmosphere transfer scheme (BATS) for the NCAR community model, NCAR technical note, NCAR, NCAR/TN-275+STR, Boulder, CO, USA, 1986. 13916

Engelen, R. and Bauer, P.: The use of variable CO_2 in the data assimilation of AIRS and IASI radiances, Q. J. Roy. Meteor. Soc., 140, 958–965, doi:10.1002/qj.919, 2011. 13931

Falge, E., Baldocchi, D., Tenhunen, J., Aubinet, M., Bakwind, P., Berbigier, P., Bernhofer, C., Burba, G., Clement, R., Davis, K., Elbers, J., Goldstein, A., Grelle, A., Granier, A., Guð-mundssonm, J., Hollinger, D., Kowalski, A., Katul, G., B. E. Lawq, Y. Malhi, T. M., Mon-sons, R., Mungert, J., Oechel, W., Paw, K. T., Pilegaardw, K., Rannik, Ü., Rebmanny, C., Suyker, A., Valentini, R., Wilson, K., and Wofsy, S.: Seasonality of ecosystem respiration and gross primary production as derived from FLUXNET measurements, Agr. Forest Meteorol., 113, 53–74, 2002. 13927

Flemming, J., Inness, A., Flentje, H., Huijnen, V., Moinat, P., Schultz, M. G., and Stein, O.: Coupling global chemistry transport models to ECMWF's integrated forecast system, Geosci. Model Dev., 2, 253–265, doi:10.5194/gmd-2-253-2009, 2009. 13911

Frankenberg, C., Aben, I., Bergamaschi, P., Dlugokencky, E. J., van Hees, R., Houweling, S., van der Meer, P., Snel, R., and Tol, P.: Global column-averaged methane mixing ratios from 2003 to 2009 as derived from SCIAMACHY: trends and variability, J. Geophys. Res., 116, D04302, doi:10.1029/2010JD014849, 2011. 13930

Geels, C., Doney, S., Dargaville, R., Brandt, J., and Christensen, J.: Investigating the sources of synoptic variability in atmospheric CO_2 measurements over the Northern Hemisphere continents: a regional model study, Tellus B, 56, 35–50, 2004. 13912, 13927, 13928

GLOBALVIEW-CO2: Cooperative Atmospheric Data Integration Project – Carbon Diox-ide, NOAA ESRL, Boulder, Colorado, available at: http://www.esrl.noaa.gov/gmd/ccgg/globalview/ (last access: 20 May 2014), 2011. 13919

Hollingsworth, A., Engelen, R., Textor, C., Benedetti, A., Boucher, O., Chevallier, F., Dethof, A., and J. Flemming, H. E., Granier, C., Kaiser, J., Morcrette, J.-J., Rayer, P., Peuch, V., Rouil, L., Schultz, M., Simmons, A., and Consortium, T. G.: Towards a monitoring and forecasting system for atmospheric composition: the GEMS project, B. Am. Meteorol. Soc., 89, 1147–1164, 2008. 13911

Hortal, M.: The development and testing of a new two-time-level semi-Lagrangian scheme (SETTLS) in the ECMWF forecast model, Q. J. Roy. Meteor. Soc., 128, 1671–1687, doi:10.1002/qj.200212858314, 2002. 13915

Jacobs, C., den Hurk, B. V., and de Bruin, H.: Stomatal behaviour and photosynthetic rate of unstressed grapevines in semi-arid conditions, Agr. Forest Meteorol., 80, 111–134, 1996. 13916

Janisková, M. and Lopez, P.: Linearized physics for data assimilation at ECMWF, in: Data As-similation for Atmospheric, Oceanic and Hydrological Applications, edited by: Park, S. K. and

Title Page

Abstract | Introduction

Conclusions | References

Tables | Figures

|◄ | ►|

◄ | ►

Back | Close

Full Screen / Esc

Printer-friendly Version

Interactive Discussion

Xu, L., vol. II, Springer-Verlag, Berlin, Heidelberg, doi:10.1007/978-3-642-35088-7, 251–286, 2013. 13914

Kaiser, J. W., Heil, A., Andreae, M. O., Benedetti, A., Chubarova, N., Jones, L., Morcrette, J.-J., Razinger, M., Schultz, M. G., Suttie, M., and van der Werf, G. R.: Biomass burning emissions estimated with a global fire assimilation system based on observed fire radiative power, Biogeosciences, 9, 527–554, doi:10.5194/bg-9-527-2012, 2012. 13917

Keeling, C., Whorf, T., Wahlen, M., and van der Plicht, J.: Interannual extremes in the rate of rise of atmospheric carbon dioxide since 1980, Letters to Nature, 375, 666–670, 1995. 13912

Keppel-Aleks, G., Wennberg, P. O., and Schneider, T.: Sources of variations in total column carbon dioxide, Atmos. Chem. Phys., 11, 3581–3593, doi:10.5194/acp-11-3581-2011, 2011. 13912, 13927

Keppel-Aleks, G., Wennberg, P. O., Washenfelder, R. A., Wunch, D., Schneider, T., Toon, G. C., Andres, R. J., Blavier, J.-F., Connor, B., Davis, K. J., Desai, A. R., Messerschmidt, J., Notholt, J., Roehl, C. M., Sherlock, V., Stephens, B. B., Vay, S. A., and Wofsy, S. C.: The imprint of surface fluxes and transport on variations in total column carbon dioxide, Biogeosciences, 9, 875–891, doi:10.5194/bg-9-875-2012, 2012. 13912

Koehler, M., Ahlgrimm, M., and Beljaars, A.: Unified treatment of dry convective and stratocumulus-topped boundary layers in the ecmwf model, Q. J. Roy. Meteor. Soc., 137, 43–57, 2011. 13915

Kretschmer, R., Gerbig, C., Karstens, U., and Koch, F.-T.: Error characterization of CO_2 vertical mixing in the atmospheric transport model WRF-VPRM, Atmos. Chem. Phys., 12, 2441–2458, doi:10.5194/acp-12-2441-2012, 2012. 13926

Krol, M., Houweling, S., Bregman, B., van den Broek, M., Segers, A., van Velthoven, P., Peters, W., Dentener, F., and Bergamaschi, P.: The two-way nested global chemistry-transport zoom model TM5: algorithm and applications, Atmos. Chem. Phys., 5, 417–432, doi:10.5194/acp-5-417-2005, 2005. 13915

Law, R., Peters, W., Rödenbeck, C., Aulagnier, C., Baker, I., Bergmann, D., Bousquet, P., Brandt, J., Bruhwiler, L., Cameron-Smith, P., Christensen, J., Delage, F., Denning, A., Fan, S., Geels, C., Houweling, S., Imasu, R., Karstens, U., Kawa, S., Kleist, J., Krol, M., Lin, S., Lokupitiya, R., Maki, T., Maksyutov, S., Niwa, Y., Onishi, R., Parazoo, N., Patra, P., Pieterse, G., Rivier, L., Satoh, M., Serrar, S., Taguchi, S., Takigawa, M., Vautard, R., Vermeulen, A., and Zhu, Z.: TransCom model simulations of hourly atmospheric

CO_2: experimental overview and diurnal cycle results for 2002, Global Biogeochem. Cy., 22, GB3009, doi:10.1029/2007gb003050, 2008a. 13912, 13915

Law, R., Peters, W., Rödenbeck, C., Aulagnier, C., Baker, I., Bergmann, D., Bousquet, P., Brandt, J., Bruhwiler, L., Cameron-Smith, P., Christensen, J., Delage, F., Denning, A., Fan, S., Geels, C., Houweling, S., Imasu, R., Karstens, U., Kawa, S., Kleist, J., Krol, M., Lin, S., Lokupitiya, R., Maki, T., Maksyutov, S., Niwa, Y., Onishi, R., Parazoo, N., Patra, P., Pieterse, G., Rivier, L., Satoh, M., Serrar, S., Taguchi, S., Takigawa, M., Vautard, R., Vermeulen, A., and Zhu, Z.: TransCom model simulations of hourly atmospheric CO_2: analysis of synoptic-scale variations for the period 2002–2003, Global Biogeochem. Cy., 22, GB3009, doi:10.1029/2007GB003081, 2008b. 13912

Le Quere, C., Raupach, M. R., Canadell, J. G., Marland, G., Bopp, L., Ciais, P., Conway, T. J., Doney, S. C., Feely, R. A., Foster, P. N., Friedlingstein, P., Gurney, K., Houghton, R. A., House, J. I., Huntingford, C., Levy, P. E., Lomas, M. R., Majkut, J., Metzl, N., Ometto, J. P., Peters, G. P., Prentice, I. C., Randerson, J. T., Running, S. W., Sarmiento, J. L., Schuster, U., Sitch, S., Takahashi, T., Viovy, N., van der Werf, G., and Woodward, F. I.: Trends in the sources and sinks of carbon dioxide, Nat. Geosci., 2, 831–836, doi:10.1038/ngeo689, 2009. 13912

Locatelli, R., Bousquet, P., Chevallier, F., Fortems-Cheney, A., Szopa, S., Saunois, M., Agusti-Panareda, A., Bergmann, D., Bian, H., Cameron-Smith, P., Chipperfield, M. P., Gloor, E., Houweling, S., Kawa, S. R., Krol, M., Patra, P. K., Prinn, R. G., Rigby, M., Saito, R., and Wilson, C.: Impact of transport model errors on the global and regional methane emissions estimated by inverse modelling, Atmos. Chem. Phys., 13, 9917–9937, doi:10.5194/acp-13-9917-2013, 2013. 13915

Masarie, K. and Tans, P.: Extension and integration of atmospheric carbon dioxide data into a globally consistent measurement record, J. Geophys. Res., 100, 11593–11610, 1995. 13951

Matross, D., Andrews, A., Pathmathevan, M., Gerbig, C., Lin, J., Wofsy, S., Daube, B., Gottlieb, E., Chow, V., Lee, J., Zhao, C., Bakwin, P., Munger, J., and Hollinger, D.: Estimating regional carbon exchange in New England and Quebec by combining atmospheric, ground-based and satellite data, Tellus B, 58, 344–358, 2006. 13931

Messerschmidt, J., Parazoo, N., Wunch, D., Deutscher, N. M., Roehl, C., Warneke, T., and Wennberg, P. O.: Evaluation of seasonal atmosphere–biosphere exchange estimations with TCCON measurements, Atmos. Chem. Phys., 13, 5103–5115, doi:10.5194/acp-13-5103-2013, 2013. 13927

Title Page

Abstract | Introduction

Conclusions | References

Tables | Figures

|◀ | ▶|

◀ | ▶

Back | Close

Full Screen / Esc

Printer-friendly Version

Interactive Discussion

Morcrette, J.-J., Boucher, O., Jones, L., Salmond, D., Bechtold, P., Beljaars, A., Benedetti, A., Bonet, A., Kaiser, J., Razinger, M., Schulz, M., Serrar, S., Simmons, A., Sofiev, M., Suttie, M., Tompkins, A., and Untch, A.: Aerosol analysis and forecast in the European Centre for Medium-Range Weather Forecasts Integrated Forecast System: forward modeling, J. Geophys. Res., 114, D06206, doi:10.1029/2008JD011235, 2009. 13911

Muñoz-Sabater, J., Fouilloux, A., and de Rosnay, P.: Technical implementation of SMOS data in the ECMWF Integrated Forecasting System, IEEE Geosci. Remote S., 9, 252–256, doi:10.1109/LGRS.2011.2164777, 2012. 13929

Muñoz-Sabater, J., de Rosnay, P., Fouilloux, A., Dahoui, M., Isaksen, L., Albergel, C., Mallas, I., and Wilhelmsson, T.: Phase I, Final Report, Tech. rep., European Centre for Medium-Range Weather Forecasts, Reading, United Kingdom, 2013. 13930

Notholt, J., Blumenstock, T., Brunner, D., Buchmann, B., Dils, B., Mazière, M. D., Popp, C., and Sussmann, R.: Product Validation Plan (PVP) Version 1 for the Essential Climate Variable (ECV): Greenhouse Gases (GHG), ESA Climate Change Initiative (CCI), available at: www.esa-ghg-cci.org (last access: 20 May 2014), 2011. 13930

Notholt, J., Blumenstock, T., Brunner, D., Buchmann, B., Dils, B., Mazière, M. D., Sussmann, R., Boesch, H., Buchwitz, M., Crevoisier, C., Detmers, R., Hasekamp, O., Laeng, A., Parker, R., Reuter, M., and Schneising, O.: Product Validation and Intercomparison Report (PVIR) for the Essential Climate Variable (ECV): Greenhouse Gases (GHG), ESA Climate Change Initiative (CCI), available at: www.esa-ghg-cci.org (last access: 20 May 2014), 2013. 13930

O'Dell, C. W., Connor, B., Bösch, H., O'Brien, D., Frankenberg, C., Castano, R., Christi, M., Eldering, D., Fisher, B., Gunson, M., McDuffie, J., Miller, C. E., Natraj, V., Oyafuso, F., Polonsky, I., Smyth, M., Taylor, T., Toon, G. C., Wennberg, P. O., and Wunch, D.: The ACOS CO_2 retrieval algorithm – Part 1: Description and validation against synthetic observations, Atmos. Meas. Tech., 5, 99–121, doi:10.5194/amt-5-99-2012, 2012. 13933

Parazoo, N., Denning, A., Berry, J., Wolf, A., Randall, A., Kawa, S., Pauluis, O., and Doney, S.: Moist synoptic transport of CO_2 along the mid-latitude storm track, Geophys. Res. Lett., 38, L09804, doi:10.1029/2011GL047238, 2011. 13912, 13927

Pillai, D., Gerbig, C., Ahmadov, R., Rödenbeck, C., Kretschmer, R., Koch, T., Thompson, R., Neininger, B., and Lavrié, J. V.: High-resolution simulations of atmospheric CO_2 over complex terrain – representing the Ochsenkopf mountain tall tower, Atmos. Chem. Phys., 11, 7445–7464, doi:10.5194/acp-11-7445-2011, 2011. 13927, 13928

Title Page

Abstract | Introduction

Conclusions | References

Tables | Figures

|◄ | ►|

◄ | ►

Back | Close

Full Screen / Esc

Printer-friendly Version

Interactive Discussion

Rabier, F., Järvinen, H., Klinker, E., Mahfouf, J.-F., and Simmons, A.: The ECMWF operational implementation of four-dimensional variational assimilation. part I: Experimental results with simplified physics, Q. J. Roy. Meteor. Soc., 126, 1143–1170, 2000. 13914

Rivier, L., Peylin, P., Ciais, P., Gloor, M., Rödenbeck, C., Geels, C., Karstens, U., Brandt, P. B. J., Heimann, M., and Aerocarb experimentalists: European CO_2 fluxes from atmospheric inversions using regional and global transport models, Climatic Change, 103, 93–115, doi:10.1007/s10584-010-9908-4, 2010. 13931

Rodgers, C. and Connor, B.: Intercomparison of remote sounding instruments, J. Geophys. Res., 108, 4116, doi:10.1029/2002JD002299, 2003. 13932

Saito, R., Patra, P., Sweeney, C., Machida, T., Krol, M., Houweling, S., Bousquet, P., Agusti-Panareda, A., Belikov, D., Bergmann, D., Bian, H., Cameron-Smith, P., Chipperfield, M., Fortems-Cheiney, A., Fraser, A., Gatti, L., Gloor, E., Hess, P., Kawa, S., Law, R., Locatelli, R., Loh, Z., Maksyutov, S., Meng, L., Miller, J., Palmer, P., Prinn, R., Rigby, M., and Wilson, C.: TransCom model simulations of methane: comparison of vertical profiles with aircraft measurements, J. Geophys. Res., 118, 1–14, doi:10.1002/jgrd.50380, 2013. 13915

Sandu, I., Beljaars, A., Bechtold, P., Mauritsen, T., and Balsamo, G.: Why is it so difficult to represent stably stratified conditions in numerical weather prediction (NWP) models?, Journal of Advances in Modeling Earth Systems, 5, 1–17, doi:10.1002/jame.20013, 2013. 13924, 13928, 13929

Schneising, O., Bergamaschi, P., Bovensmann, H., Buchwitz, M., Burrows, J. P., Deutscher, N. M., Griffith, D. W. T., Heymann, J., Macatangay, R., Messerschmidt, J., Notholt, J., Rettinger, M., Reuter, M., Sussmann, R., Velazco, V. A., Warneke, T., Wennberg, P. O., and Wunch, D.: Atmospheric greenhouse gases retrieved from SCIAMACHY: comparison to ground-based FTS measurements and model results, Atmos. Chem. Phys., 12, 1527–1540, doi:10.5194/acp-12-1527-2012, 2012. 13931

Schuh, A. E., Denning, A. S., Corbin, K. D., Baker, I. T., Uliasz, M., Parazoo, N., Andrews, A. E., and Worthy, D. E. J.: A regional high-resolution carbon flux inversion of North America for 2004, Biogeosciences, 7, 1625–1644, doi:10.5194/bg-7-1625-2010, 2010. 13931

Stephens, B., Gurney, K., Tans, P., Sweeney, C., Peters, W., Bruhwiler, L., Ciais, P., Ramonet, M., Bousquet, P., Nakazawa, T., Aoki, S., Machida, T., Inoue, G., Binnichenko, N., lloyd, J., Jordan, A., Heimann, M., Shibistova, O., Langenfelds, R., Steele, L., Francey, R., and Denning, A.: Weak northern and strong tropical land carbon uptake from vertical profiles of atmospheric CO_2, Science, 316, 1732–1735, doi:10.1126/science.1137004, 2007. 13926

Takahashi, T., Sutherland, S., Wanninkhof, R., Sweeney, C., Feely, R., Chipman, D., Hales, B., Friederich, G., Chavez, F., Watson, A., Bakker, D., Schuster, U., Metzl, N., Yoshikawa-Inoue, H., Ishii, M., Midorikawa, T., Nojiri, Y., Sabine, C., Olafsson, J., Arnarson, T., Tilbrook, B., Johannessen, T., Olsen, A., Bellerby, R., Körtzinger, A., Steinhoff, T.,
Hoppema, M., de Baar, H., Wong, C., Delille, B., and Bates, N. R.: Climatological mean and decadal changes in surface ocean pCO_2, and net sea-air CO_2 flux over the global oceans, Deep-Sea Res. Pt. II, 56, 554–577, 2009. 13917

Tans, P., Bakwin, P. S., Conway, T. J., Dissly, R. W., Dlugokencky, E. J., Geller, L. S., Guenther, D. W., Hurst, D. F., Kitzis, D. R., Lang, P. M., Masarie, K. A., Miller, J. B., Novelli, P. C., Prostko-
Bell, C., Ramonet, M., Thoning, K. W., Trolier, M., Waterman, L. S., Zhang, N., and Zhao, C.: Carbon Cycle (Group Report), Summary Report 1994–1995, Tech. Rep. 23, edited by: Hoffman, D. J., Peterson, J. T., and Rosson, R. M., US Department of Commerce, Climate Monitoring and Diagnostics Laboratory, Boulder, Colorado, 1996. 13917, 13962

Thoning, K., Kitzis, D., and Crotwell, A.: Atmospheric Carbon Dioxide Dry Air Mole Fractions from quasi-continuous measurements at Barrow, Alaska; Mauna Loa, Hawaii; American Samoa; and South Pole, 1973–2011, Version: 2012-05-07, Tech. Rep., available at: ftp://aftp.cmdl.noaa.gov/data/greenhouse_gases/co2/in-situ/ (last access: 20 May 2014), NOAA, 2012. 13917, 13919

Tiedtke, M.: A comprehensive mass flux scheme for cumulus parameterization in large-scale models, Mon. Weather Rev., 117, 1779–1800, 1989. 13915

Untch, A. and Hortal, M.: A finite-element scheme for the vertical discretization of the semi-Lagrangian version of the ECMWF forecast model, Q. J. Roy. Meteor. Soc., 130, 1505–1530, doi:10.1256/qj.03.173, 2006. 13915

Wofsy, S.: HIAPER Pole-to-Pole Observations (HIPPO): fine-grained, global-scale measurements of climatically important atmospheric gases and aerosols, Philos. T. R. Soc. A, 369, 2073–2086, doi:10.1098/rsta.2010.0313, 2011. 13925

Wofsy, S. C., Daube, B. C., Jimenez, R., Kort, E., Pittman, J. V., Park, S., Commane, R., Xiang, B., Santoni, G., Jacob, D., Fisher, J., Pickett-Heaps, C., Wang, H., Wecht, K., Wang, Q.-Q., Stephens, B. B., Shertz, S., Watt, A., Romashkin, P., Campos, T., Haggerty, J.,
Cooper, W. A., Rogers, D., Beaton, S., Hendershot, R., Elkins, J. W., Fahey, D. W., Gao, R. S., Moore, F., Montzka, S. A., Schwarz, J. P., Perring, A. E., Hurst, D., Miller, B. R., Sweeney, C., Oltmans, S., Nance, D., Hintsa, E., Dutton, G., Watts, L. A., Spackman, J. R., Rosenlof, K. H., Ray, E. A., Hall, B., Zondlo, M. A., Diao, M., Keeling, R., Bent, J., Atlas, E. L., Lueb, R., and

Title Page

Abstract | Introduction

Conclusions | References

Tables | Figures

|◄ | ►|

◄ | ►

Back | Close

Full Screen / Esc

Printer-friendly Version

Interactive Discussion

Mahoney, M. J.: HIPPO Merged 10-second Meteorology, Atmospheric Chemistry, Aerosol Data, Tech. Rep. Release 20121129, Carbon Dioxide Information Analysis Center, Oak Ridge National Laboratory, Oak Ridge, Tennessee, USA, doi:10.3334/CDIAC/hippo_010, 2012. 13917, 13925

5 Wunch, D., Toon, G. C., Wennberg, P. O., Wofsy, S. C., Stephens, B. B., Fischer, M. L., Uchino, O., Abshire, J. B., Bernath, P., Biraud, S. C., Blavier, J.-F. L., Boone, C., Bowman, K. P., Browell, E. V., Campos, T., Connor, B. J., Daube, B. C., Deutscher, N. M., Diao, M., Elkins, J. W., Gerbig, C., Gottlieb, E., Griffith, D. W. T., Hurst, D. F., Jiménez, R., Keppel-Aleks, G., Kort, E. A., Macatangay, R., Machida, T., Matsueda, H., Moore, F., Morino, I.,

10 Park, S., Robinson, J., Roehl, C. M., Sawa, Y., Sherlock, V., Sweeney, C., Tanaka, T., and Zondlo, M. A.: Calibration of the Total Carbon Column Observing Network using aircraft profile data, Atmos. Meas. Tech., 3, 1351–1362, doi:10.5194/amt-3-1351-2010, 2010. 13932

Wunch, D., Toon, G. C., Blavier, J.-F. L., Washenfelder, R. A., Notholt, J., Connor, B., Griffith, D. W. T., Sherlock, V., and Wennberg, P. O.: The total carbon column observing network,

15 Philos. T. R. Soc. A, 369, 2087–2112, doi:10.1098/rsta.2010.0240, 2011. 13917

Table 1. Stations with continuous and total column sampling of CO$_2$ used to evaluate the CO$_2$ hindcast.

Site	Name (Country)	Latitude	Longitude	Altitude [masl]	Sampling type	Observing Network	Baseline Obs.
BRW	Barrow (USA)	71.32° N	156.61° W	11	surface	ESRL/NOAA	yes
SMO	American Samoa (USA)	14.25° S	170.56° W	42	surface	ESRL/NOAA	yes
SPO	South Pole (USA)	89.98° S	24.80° W	2810	surface	ESRL/NOAA	yes
AMT	Argyle (USA)	45.03° N	68.68° W	50	tall tower	ESRL/NOAA	no
LEF	Park Falls (USA)	45.95° N	90.27° W	472	tall tower	ESRL/NOAA	no
WBI	West Branch (USA)	41.73° N	91.35° W	242	tall tower	ESRL/NOAA	no
	Bialystok (Poland)	53.23° N	23.03° E	180	total column	TCCON	no
	Sodankylä (Finland)	67.37° N	26.63° E	180	total column	TCCON	no
	Lamont (USA)	36.60° N	97.49° W	320	total column	TCCON	no
	Lauder (New Zeland)	45.04° S	169.68° E	370	total column	TCCON	no
	Wollongong (Australia)	34.41° S	150.88° E	30	total column	TCCON	no
	Parkfalls (USA)	45.95° N	90.27° W	440	total column	TCCON	no
CBW	Cabauw (Netherlands)	51.97° N	4.93° E	0	tall tower	ICOS	no
IVI	Ivitutt (Greenland)	61.21° N	48.17° W	16	surface	ICOS	no
LTO	Lamto (Ivory Coast)	6.22° N	5.03° W	155	surface	ICOS	no
MHD	Mace Head (Ireland)	53.33° N	9.90° W	25	surface	ICOS	no
PUJ	Puijo (Finland)	62.0° N	27.0° E	232	surface	ICOS	no

Title Page

Abstract | Introduction

Conclusions | References

Tables | Figures

|◀ | ▶|

◀ | ▶

Back | Close

Full Screen / Esc

Printer-friendly Version

Interactive Discussion

Table 2. Correlation between observed and modelled daily mean CO$_2$ at several sites from the NOAA/ESRL tower network. Correlation coefficient values are significant at the 90 % level, dashes indicating the correlation coefficients are not significant. Station locations and sampling heights are shown in Tables 1 and 3.

Site	Jan	Feb	Mar	Apr	May	Jun	Jul	Aug	Sep	Oct	Nov	Dec
AMT1	0.91	0.84	0.71	0.71	0.40	–	0.45	0.42	0.86	0.69	0.84	0.91
AMT2	0.93	0.84	0.70	0.66	0.41	–	0.56	0.32	0.88	0.72	0.64	0.91
AMT3	0.94	0.75	0.52	–	–	0.43	0.51	0.49	0.89	0.83	0.47	0.90
LEF2	0.91	0.79	–	–	0.43	0.44	0.70	0.64	0.49	0.79	0.66	0.68
LEF4	0.93	0.88	–	−0.60	–	0.55	0.82	0.75	0.77	0.77	0.78	0.86
LEF6	0.95	0.89	−0.43	−0.37	0.52	0.66	0.85	0.78	0.81	0.76	0.72	0.90
WBI1	0.63	0.70	–	–	–	0.49	0.54	0.51	0.57	0.65	0.74	0.68
WBI2	0.63	0.82	–	−0.33	–	0.58	0.71	0.74	0.56	0.70	0.74	0.76
WBI3	0.81	0.92	–	–	–	0.68	0.81	0.78	0.56	0.72	0.77	0.77

Table 3. Sampling heights at the tall towers listed in Table 2.

Site ID sampling level	Station (Country)	Sampling height [m]	Network
AMT1	Argyle (USA)	12	ESRL/NOAA
AMT2		30	
AMT3		107	
LEF2	Park Falls (USA)	30	ESRL/NOAA
LEF4		122	
LEF6		396	
WBI1	West Branch (USA)	31	ESRL/NOAA
WBI2		99	
WBI3		379	

Table 4. Correlations between detrended hindcast and observed CO$_2$ at two different levels of the Park Falls tall tower showing the impact of synoptic variability of NEE on the atmospheric CO$_2$ hindcast.

NEE flux	Daytime CO$_2$ minimum (30 m)	Daytime CO$_2$ minimum (396 m)	Nightime CO$_2$ maximum (30 m)	Nightime CO$_2$ maximum (396 m)	CO$_2$ daily mean (30 m)	CO$_2$ daily mean (396 m)
with synoptic variability	0.43	0.57	0.49	0.86	0.64	0.84
without synoptic variability	0.26	0.52	0.45	0.93	0.53	0.89
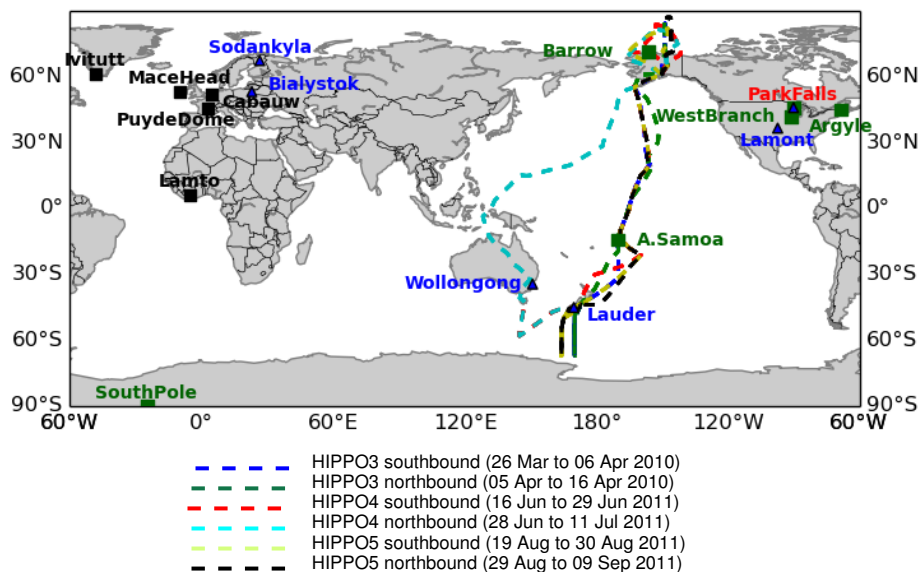
Figure 1. Maps showing the location of stations with continuous surface measurements from the NOAA/ESRL network (green squares), the ICOS network (black squares), the total column FTIR stations from the TCCON network (blue triangles) and the HIPPO flight tracks used in the evaluation of the CO_2 hindcast (dashed lines, see flight period in the legend). Note that Park Falls (in red) has both total column TCCON observations as well as tall tower observations from the ESRL/NOAA network.

Title Page

Abstract   Introduction

Conclusions   References

Tables   Figures

◄   ►

◄   ►

Back   Close

Full Screen / Esc

Printer-friendly Version

Interactive Discussion
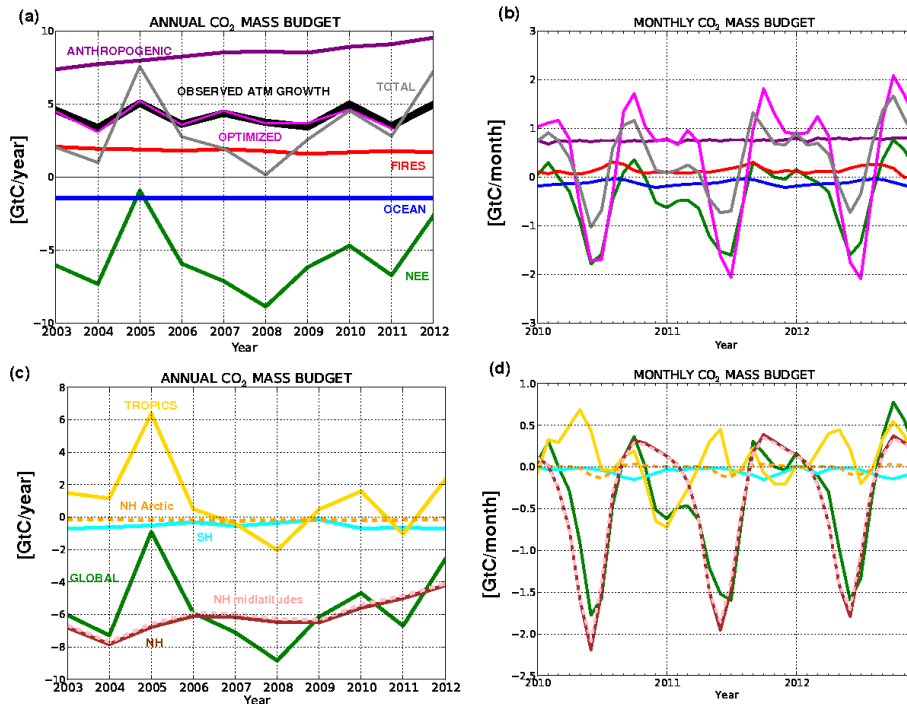
Figure 2. (a) Annual and **(b)** monthly global CO_2 budget for the modelled total CO_2 flux (grey) compared to the observed CO_2 atmospheric growth from NOAA (black) from 2003 to 2012 and from 2010 to 2012 respectively. The different flux components are shown by the other coloured lines: anthropogenic (purple), fires (red), ocean (blue) amd land vegetation (green). The optimized total CO_2 fluxes from Chevallier et al. (2011) are shown in magenta; (**c** and **d**) depict the NEE annual and monthly budgets respectively for different regions: global in green, tropics (between 30° S and 30° N) in yellow, Southern Hemisphere (south of 30° S) in blue, NH (north of 30° N) in brown, NH mid-latitudes (between 30° N and 66° N) in dashed pink and NH arctic (north of 66° N) in dashed orange.

Title Page

Abstract | Introduction

Conclusions | References

Tables | Figures

|◄ | ►|

◄ | ►

Back | Close

Full Screen / Esc

Printer-friendly Version

Interactive Discussion

Figure 3. NOAA GLOBALVIEW CO$_2$ (2011) product for 2010 based on observations (left) compared to the equivalent product based on the atmospheric CO$_2$ hindcast (middle). The difference between the GLOBALVIEW product based on observations and model is shown in the right panel. The CO$_2$ hindcast has been sampled at the same locations as the GLOBALVIEW observations and the same data processing described in Masarie and Tans (1995) has been applied.

Figure 4. Monthly bias (hindcast – observation) of CO_2 dry molar fraction [ppm] at NOAA/ESRL continuous surface sites sampling background air (green triangles) and differential monthly biases (i.e. difference of monthly bias with respect to previous month) as red triangles from 2003 to 2011. The blue dots highlight the adjustment in CO_2 at the beginning of each year when the model is re-initialized with a simulation from optimized fluxes which has a bias close to zero (see text for details).

Discussion Paper | Discussion Paper | Discussion Paper | Discussion Paper

Title Page

Abstract | Introduction

Conclusions | References

Tables | Figures

|◄ | ►|

◄ | ►

Back | Close

Full Screen / Esc

Printer-friendly Version

Interactive Discussion
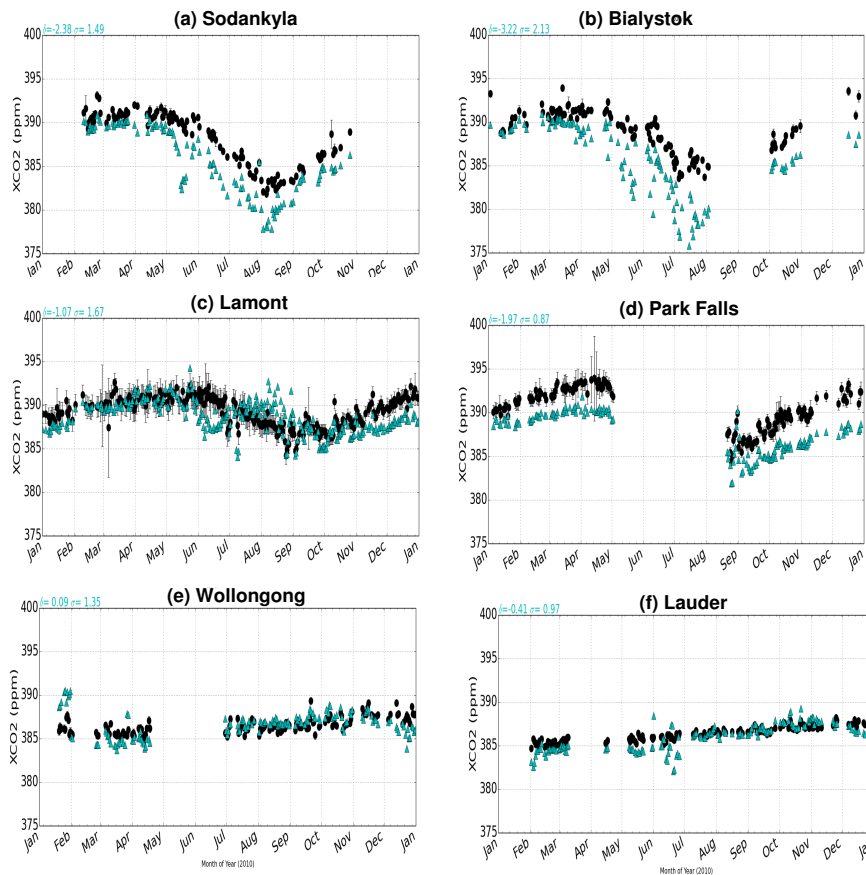
Figure 5. Daily mean total column dry molar fraction [ppm] of CO_2 at TCCON sites from measurements (dark circles) and hindcast (blue triangles) in 2010. Error bars indicate the uncertainty associated with observations. The delta and the sigma values are the mean and standard deviation of the model minus TCCON data.

Title Page

Abstract | Introduction

Conclusions | References

Tables | Figures

|◄ | ►|

◄ | ►

Back | Close

Full Screen / Esc

Printer-friendly Version

Interactive Discussion
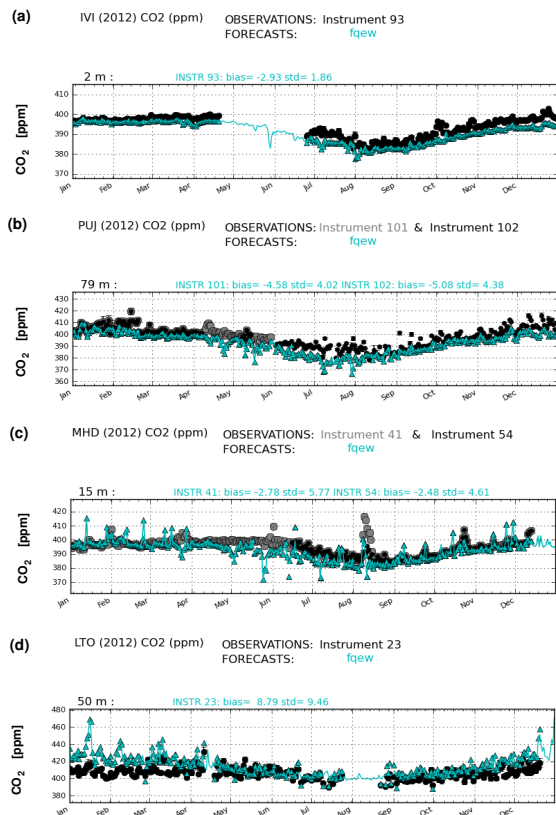
Figure 6. Daily mean dry molar fraction [ppm] of CO_2 at ICOS continuous surface sampling sites from measurements (black and grey circles represent two different instruments) and hindcasts collocated in time and space with observations (blue triangles) in 2012. The blue line depicts the daily mean values computed from the 3 hourly model data. Any departures between the blue triangles and the blue line indicate that the observations are not able to sample the true daily mean. Error bars indicate the uncertainty associated with observations.
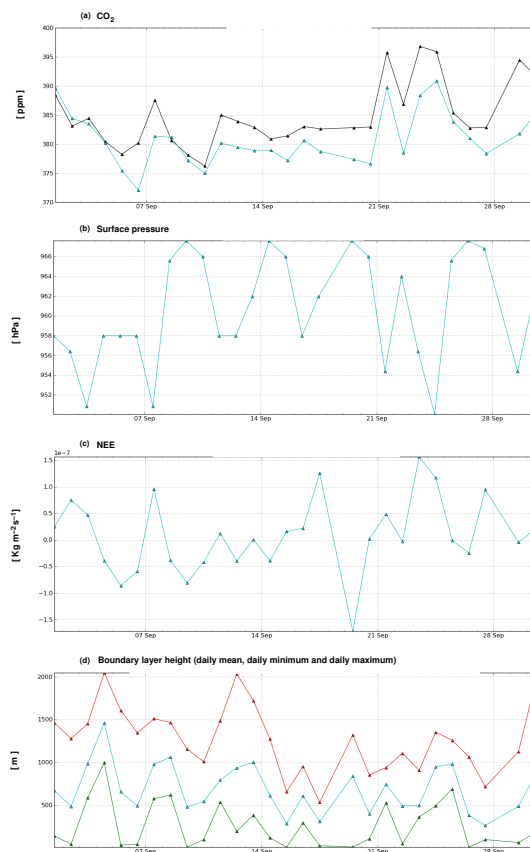
Figure 7. (a) Daily mean dry molar fraction [ppm] of CO_2 from measurements (dark circles) and model (cyan triangles); **(b)** daily mean surface pressure [hPa]; **(b)** daily mean modelled NEE [kg m^{-2} s^{-1}]; and **(d)** daily mean, minimum and maximum boundary layer height [m] (cyan, blue, red) at the Park Falls NOAA/ESRL tall tower in September 2010.
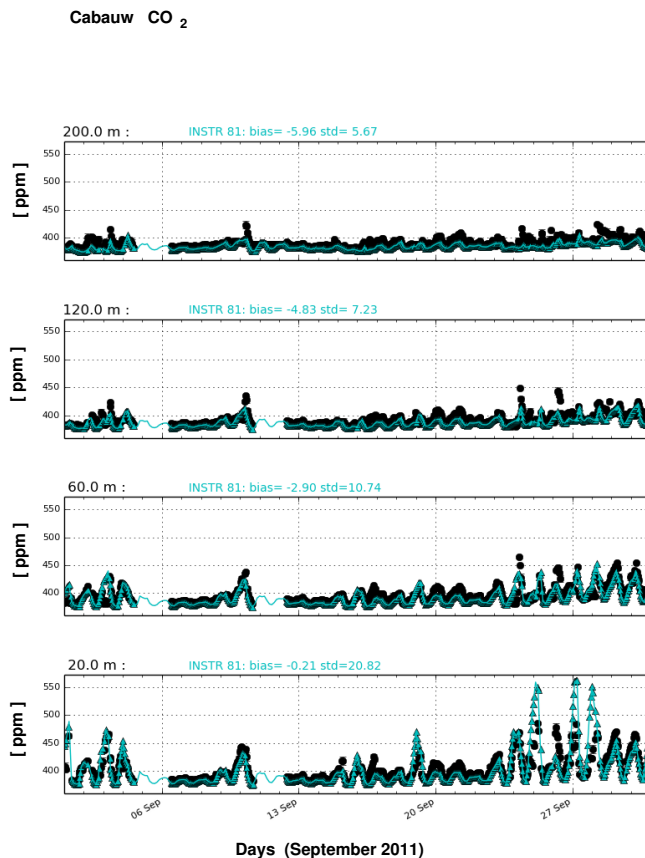
Title Page

Abstract | Introduction

Conclusions | References

Tables | Figures

|◄ | ►|

◄ | ►

Back | Close

Full Screen / Esc

Printer-friendly Version

Interactive Discussion
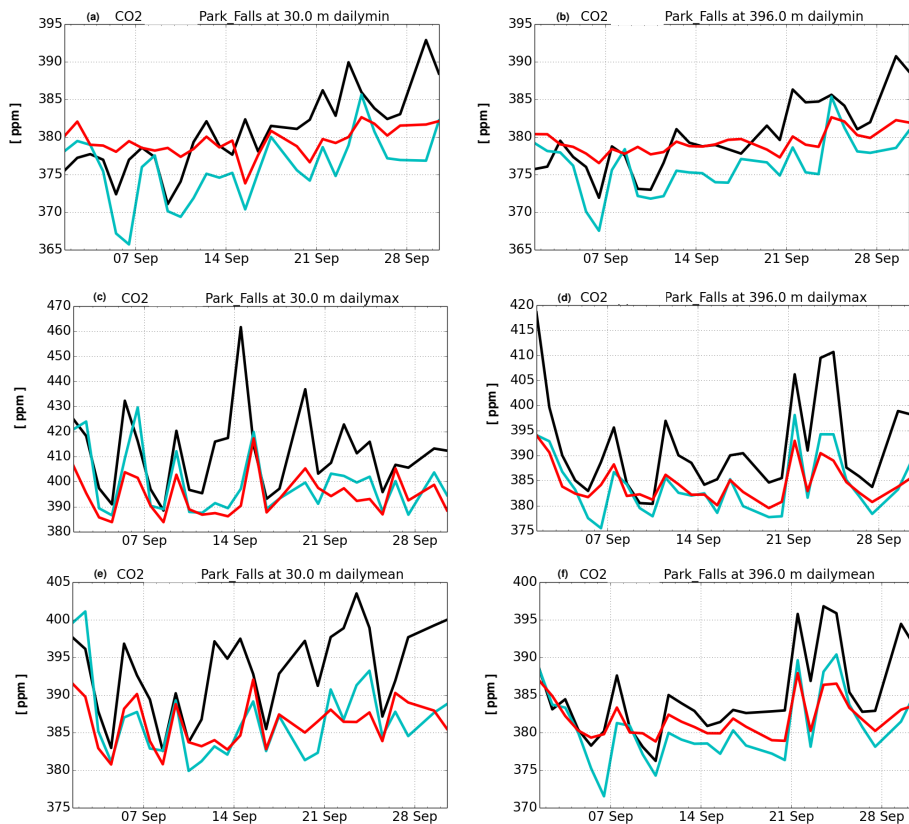
Figure 8. Daily minimum, maximum and mean atmospheric CO_2 at Park Falls (Winsconsin, USA) at 30 m (left panels) and 396 m (right panels) from observations in black, the hindcast with NEE synoptic variability in light blue and the simulation with monthly mean NEE in red for September 2010.
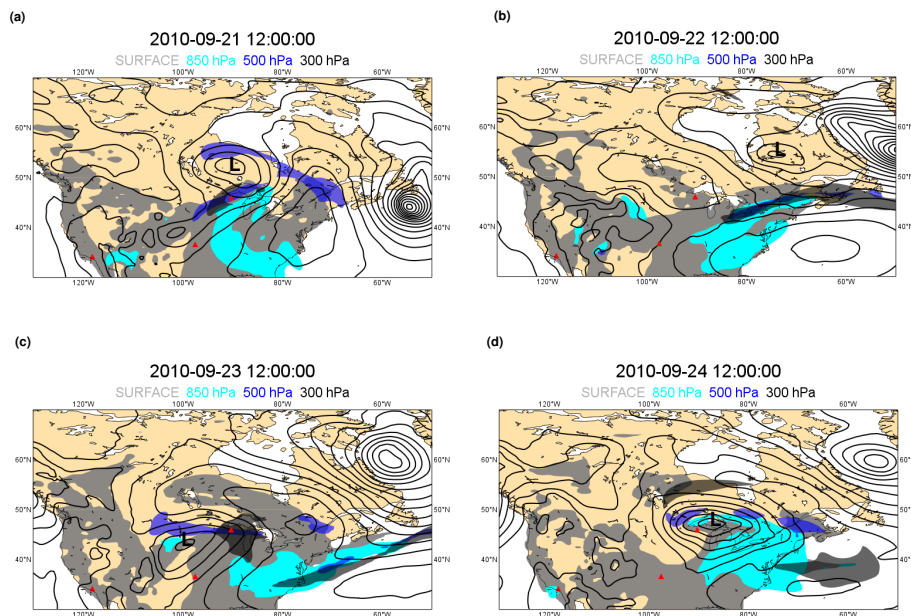
Figure 9. Transport of atmospheric CO_2 anomalies associated with the passage of low pressure systems over North America. The colours depict the CO_2 anomalies anomalies above the well-mixed background CO_2 at different vertical levels: grey near the surface, cyan at 850 hPa, blue at 500 hPa and dark grey at 300 hPa. The anomalies are defined as CO_2 dry molar fraction above the background value of 392 ppm for both near the surface and at the 850 hPa level; and above the background value of 388 ppm for the 500 and 300 hPa levels. The location of the TCCON sites are depicted by a red triangle. The black contours of mean sea level pressure show the location of the centre of the low pressure systems (L).

Title Page

Abstract | Introduction

Conclusions | References

Tables | Figures

|◄ | ►|

◄ | ►

Back | Close

Full Screen / Esc

Printer-friendly Version

Interactive Discussion

Figure 10. Hourly mean CO_2 dry molar fraction [ppm] at the ICOS site at Cabauw (Netherlands) from measurements (dark circles) and hindcast (blue triangles) in September 2011 at several sampling heights. The solid blue line shows the hourly values of the CO_2 hindcast even in the absence of observations. The values for the bias and standard deviation [ppm] are shown in the title above each panel.

Title Page

Abstract | Introduction

Conclusions | References

Tables | Figures

Back | Close

Full Screen / Esc

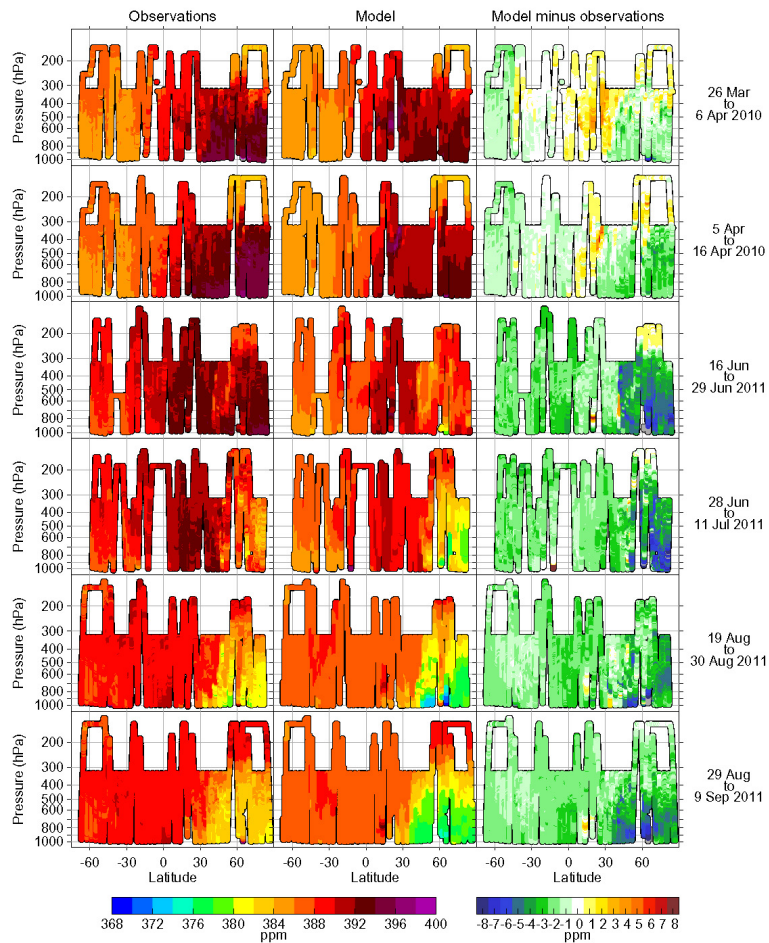Printer-friendly Version

Interactive Discussion
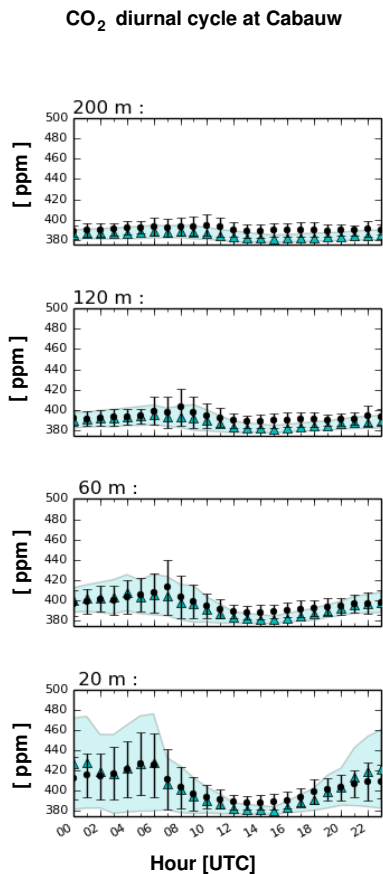
Figure 11. Mean diurnal cycle of CO_2 dry molar fraction [ppm] at the ICOS site at Cabauw (Netherlands) from measurements (dark circles) and hindcast (blue triangles) in September 2011 at several sampling heights. The standard deviation of observations and hindcast are shown as black bars and blue shading respectively.

Title Page

Abstract | Introduction

Conclusions | References

Tables | Figures

|◄ | ►|

◄ | ►

Back | Close

Full Screen / Esc

Printer-friendly Version

Interactive Discussion
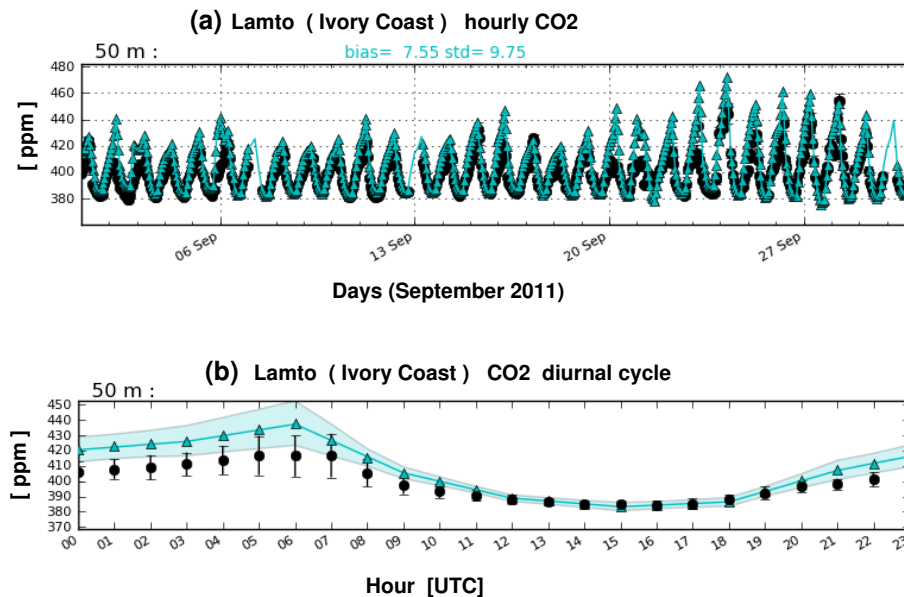
Figure 12. (a) Hourly mean dry molar fraction of CO$_2$ [ppm] and **(b)** its mean diurnal cycle at the ICOS site at Lamto (Ivory Coast) from measurements (dark circles) and hindcast (blue triangles) in September 2011. The standard deviation of observations and hindcast are shown as black bars and blue shading respectively. The solid blue line in **(a)** shows the hourly values of the CO$_2$ hindcast even in the absence of observations and in **(b)** the mean diurnal cycle in the CO$_2$ hindcast.
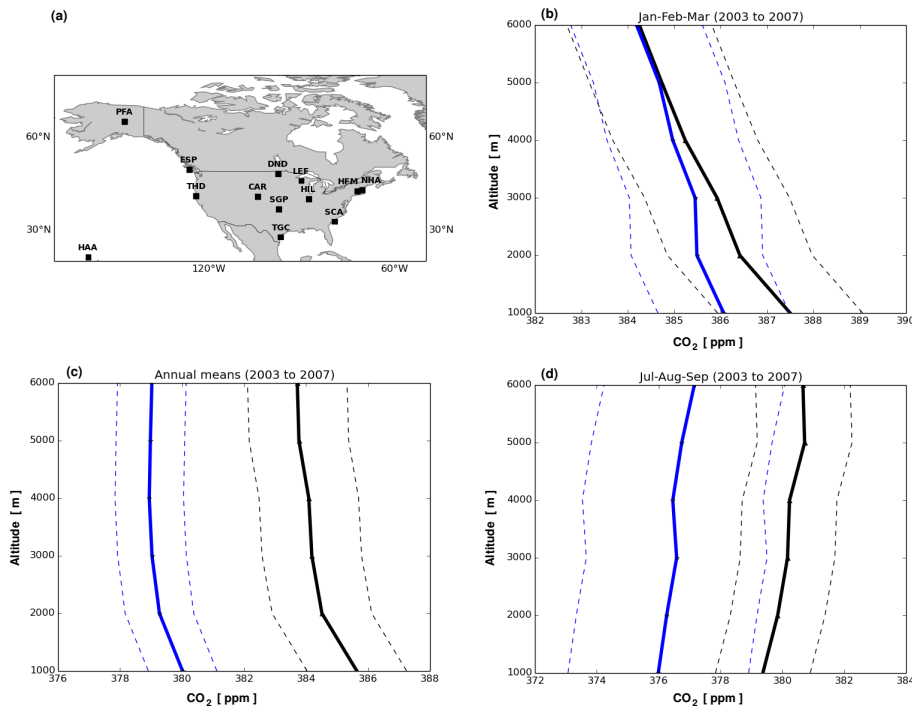
Full Screen / Esc

Printer-friendly Version

Interactive Discussion

Figure 13. CO$_2$ dry molar fraction [ppm] from HIPPO flights and CO$_2$ hindcast in 2010 and 2011. Flight tracks are shown in Fig. 1.

Figure 14. Average profiles of CO_2 dry molar fraction [ppm] observed by NOAA/ESRL GMD Carbon Cycle Vertical Profile Network (Tans et al., 1996) in black and CO_2 hindcast in blue from 2003 to 2007. The standard deviation of the profiles is shown as dashed lines.

Title Page

Abstract | Introduction

Conclusions | References

Tables | Figures

|◀ | ▶|

◀ | ▶

Back | Close

Full Screen / Esc

Printer-friendly Version

Interactive Discussion